This article can be cited before page numbers have been issued, to do this please use: Z. Peng, S. Yilu, I. En-Naji, A. Khojastehnezhad and M. Siaj, *Chem. Commun.*, 2026, DOI: 10.1039/D5CC05030H.

ARTICLE

Low-dimensional transition metal dichalcogenides heterostructure photoanodes for photoelectrochemical hydrogen evolution application: Recent progress and prospects

Zhiyuan Peng,[a,†] Yilu Su,[b,†] Imane En-Naji,[a] Amir Khojastehnezhad [a] and Mohamed Siaj [a,*]

Solar-driven hydrogen evolution through photoelectrochemical (PEC) water splitting technology provides a prospective approach for green energy production. To accomplish reliable PEC systems with sufficient solar-to-hydrogen conversion efficiencies (STH, ≥10%), one of current primary challenges lies in the design and fabrication of highly-performing semiconductor (SC) photoanodes to overcome its high overpotential requirement and sluggish surface oxidation kinetics. The emerging of low-dimensional layered transition metal dichalcogenides (TMDs) with extraordinary electronic and optical properties has gained considerable attention and been inarguably promising photoanode candidates. The rational combination of TMDs interfaced with other SC photoabsorbers via energy band modulation and heterojunction formation can markedly improve PEC performance and solar conversion. In the context, this review begins with the description of PEC water oxidation mechanism, efficiency-related parameters, band bending and charge transfer behavior within n-type SC photoanodes, followed by an overview of recent progress and our contributions in fabricating efficient TMDs-based heterostructure photoanodes with various synthetic routes and architectures. Next, the unique superiorities and positive effects of TMDs utilization, such as optimized light harvesting, regulated electron transfer channels, promoted charge separation and transport, and improved long-term photostability, were comprehensively summarized in various TMDs/SC heterostructure photoanode systems. Finally, the remaining challenges and future opportunities in advancing TMDs-based van der Waals heterostructure photoanodes for next generation PEC water splitting application are addressed.

1. Introduction

Developing a global-scale green hydrogen economy is one of the most promising strategies to address the escalating energy supply challenges facing humanity and decarbonize. According to the Statistical Review of World Energy in 2024, approximately 81.3% of total energy demand relies on the extensive combustion of non-renewable fossil fuels (e.g., oil, coal, and natural gas), leading to energy shortages and environmental degradation. Therefore, a swift transition from traditional fossil fuels to clean and sustainable energy sources is imperative. Hydrogen (H_2), known for its eco-friendly characteristic of zero carbon emissions and excellent gravimetric heating value (142 MJ kg^{-1}), is poised to be a viable alternative energy source.[1-3] Sunlight-driven hydrogen generation through photoelectrochemical (PEC) water-splitting can directly convert renewable solar energy into storable hydrogen fuel in an environmentally friendly and cost-effective manner, attracting significant research interest.[4] In a typical PEC system, semiconductor electrodes are photoexcited to generate electron-hole pairs under sunlight irradiation, driving the photocathodic hydrogen

evolution reaction (HER) and the photoanodic oxygen evolution reaction (OER). Compared with conventional powder photocatalytic or photovoltaic-electrocatalytic hydrolysis, this system accomplishes direct solar-to-hydrogen (STH) conversion with a subtle balance between energy efficiency and device complexity. Over the past decades, PEC water splitting technology has achieved significant progress but is still far from industrial scale-up due to insufficient STH efficiency and long-term durability. Overcoming these limitations necessitates ongoing innovation in photoelectrode fabrication and device architecture.[5] Noteworthily, relative to HER, the OER is particularly complex, involving a four-proton coupled electron exchange process, which necessitates a photoanode with superior charge transfer and injection properties to overcome the higher overpotential requirement and sluggish oxidation kinetics.[6, 7] Despite substantial efforts to enhance photoanodes, the OER remains the rate-limiting step and a major bottleneck in overall PEC water splitting.

An ideal OER photoanode should be low-cost, physiochemically stable, and possess a suitable energy band structure that allows for visible-light absorption and effective water oxidation. On the basis of these principles, low-dimensional transition metal dichalcogenides (TMDs), especially two-dimensional (2D) TMDs, have been thoroughly investigated and present great potential in energy harvesting, conversion, and storage applications because of their narrow bandgaps, large surface-to-volume atomic ratio, stackability, high charge mobility, short

a. Faculty of Engineering, Université de Sherbrooke, 2500 Blvd de l'Université, Sherbrooke, QC, J1K 2R1, Canada.
b. Department of Chemistry, Université du Québec à Montréal, Montréal, QC, H3C 3P8, Canada.
† These authors contributed equally.
* Corresponding author, E-mail: mohamed.siaj@usherbrooke.ca.

carrier diffusion distance, and thickness-dependent photoelectronic properties.[8-10] Specifically, TMDs crystallize in a layered structure comprising a transition metal plane sandwiched by two chalcogen planes, where adjacent layers are held together via weak van der Waals forces. Such interactions facilitate easy exfoliation of TMDs materials into their few/mono layer, which generally exhibit superior conductivity, mechanical robustness, and structural stability, along with an indirect-to-direct bandgap transition relative to their bulk phase.[11-13] In addition, the diverse combinations of transition metals (Mo, W, Ti) and chalcogen atoms (S, Se, Te) give TMDs versatile structural phases, where variations in atomic coordination yield metallic, semiconducting, or semimetallic properties.[14] Thanks to these unique and extraordinary properties, low-dimensional layered TMDs have emerged as promising photoanode materials. However, in many cases, the single-component TMDs photocatalysts show non-photoactive to very weak PEC performance due to the low utilization of solar energy and high recombination of photogenerated charge carriers. Fabricating TMDs-based heterostructure photoanodes with synergistic effects, through rationally integrated with secondary photoabsorbers to form multi-heterojunction, p–n junction, or Schottky junction, are capable of effectively broadening spectrum absorption, boosting charge separation and transfer behavior, promoting surface reaction, and improving long-term stability, which has been deemed as one of the most prevalent strategies to optimize photoanode for enhanced PEC conversion efficiency.[13, 15-17]

This feature article majorly focuses on the photoanodic water oxidation reaction and describes PEC water splitting mechanism, performance parameters, band bending and charge transfer behaviour within SC photoanodes in detail. Recent progress and our contributions in designing and fabricating TMDs-based heterostructure photoanodes for efficient PEC water splitting are systematically reviewed and summarized. A particular emphasis on relevant synthetic methods and crucial roles of TMDs as photosensitizers, electron transporting mediators, passivation layers, cocatalysts, and protective layers in various TMDs/SC heterostructure PEC systems are also presented. Finally, critical outlook on the future development of highly-efficient and stable TMDs-based photoanodes, and construction of tandem devices for unassisted solar water splitting are discussed.

2. Principles of PEC water splitting

PEC water splitting for hydrogen production is driven by the photoexcited charge carriers-induced redox reactions of water.[18] Thermodynamically, the overall process of converting a water molecule into hydrogen and oxygen is energetically uphill, requiring a Gibbs free energy change of approximately 237 kJ/mol under standard conditions, which corresponds to a Nernstian potential of 1.23 V.[19-21] The complete photo-assisted water splitting involves two fundamental half-reactions: a two-electron proton reduction and a four-electron water oxidation, which are represented by the following equations:[1]
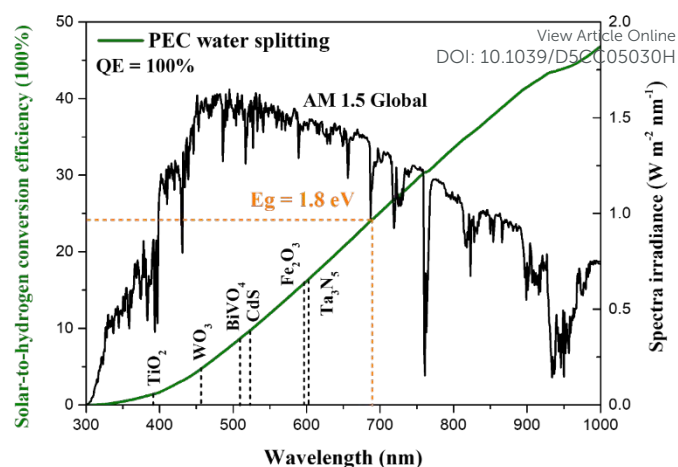
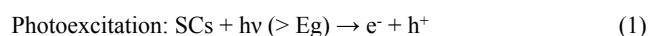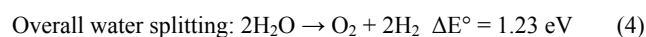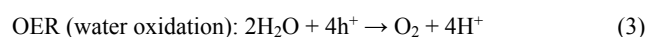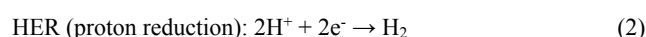Photoexcitation: $SCs + h\nu\ (> Eg) \rightarrow e^- + h^+$ (1)

Fig. 1 Air Mass 1.5 Global solar spectrum (black) with the theoretical maximum STH efficiency at 1.8 eV (green) and bandgaps of some representative photoanode materials.

HER (proton reduction): $2H^+ + 2e^- \rightarrow H_2$ (2)

OER (water oxidation): $2H_2O + 4h^+ \rightarrow O_2 + 4H^+$ (3)

Overall water splitting: $2H_2O \rightarrow O_2 + 2H_2$ $\Delta E° = 1.23\ eV$ (4)

Herein, semiconductor-based photoabsorbers (SCs) are the fundamental components enabling solar-to-hydrogen conversion. The intrinsic redox potential of water establishes both the minimum bandgap requirement and the energy band alignment necessary for this process. In principle, water splitting requires absorption of photons with energies greater than 1.23 eV, corresponding to solar wavelengths below ~1000 nm, thereby necessitating a SC bandgap (Eg) larger than 1.23 eV. Beyond this thermodynamic threshold, the band-edge positions must also be suitably aligned: the conduction band minimum (CBM) should be more negative than the hydrogen reduction potential ($E°(H^+/H_2) = 0\ V\ vs\ RHE\ (V_{RHE})$), while the valence band maximum (VBM) must be more positive than the oxygen evolution potential ($E°(O_2/H_2O) = 1.23\ V_{RHE}$).[22] In practice, however, additional energy is required to overcome kinetic overpotentials (typically 0.4–0.6 eV for both half-reactions) and to compensate for thermodynamic losses during charge carrier separation and transport (approximately 0.3–0.4 eV). Consequently, a practical bandgap of at least ~1.8 eV (spectrum absorption range up to 688 nm) for a single semiconductor is generally considered to drive overall water splitting efficiently.[19] This finding matches well with the energy density distribution of solar spectrum, in which visible region accounts for the predominant fraction (~43%). Fig. 1 provides a schematic comparison of the spectra absorption regions of several widely used SC photoanode materials, alongside the corresponding theoretical maximum STH efficiencies calculated under the assumption of 100% quantum efficiency. Among them, Ta_3N_5 stands out as one of the most promising single-absorber photoanodes for practical PEC hydrogen production, offering a high theoretical STH conversion efficiency of approximately 15%.[23-25] Fully harnessing its thermodynamic potential, especially lowering the onset potential, remains a current major
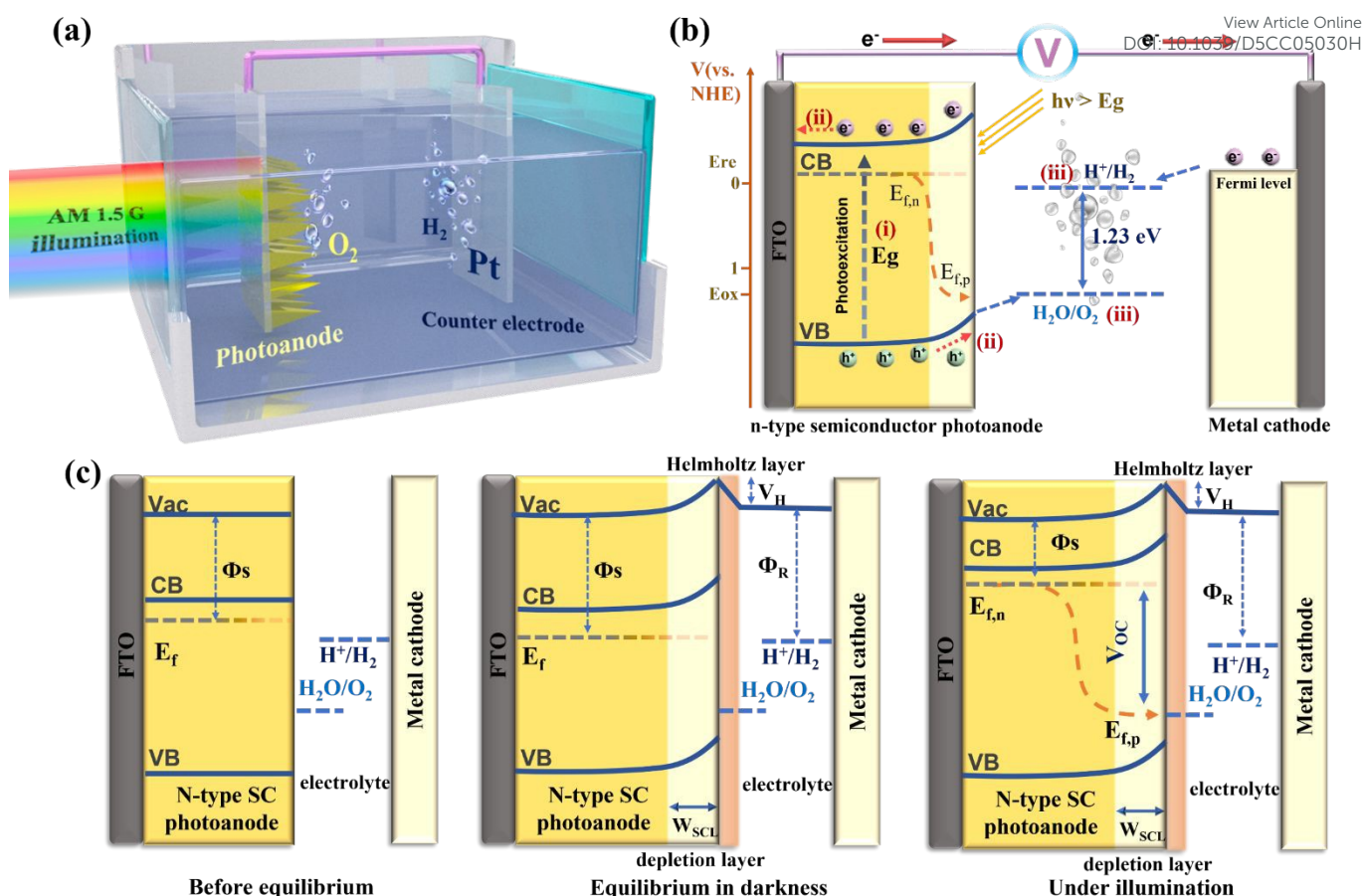
Journal Name ARTICLE

Fig. 2 (a) The schematic illustration for the configuration of a photoanode-based PEC water splitting system with AM 1.5G illumination as the solar source. (b) Working principles of an n-type semiconductor photoanode-based PEC system: (ⅰ) Photoexcitation process (E_g); (ⅱ) Charge carrier separation and transfer process; (ⅲ) Surface redox reaction. (c) Band energetics at the photoanode/electrolyte interface: before equilibration, after dark equilibration, and during quasi-static equilibration under illumination. Herein, Φ_S and Φ_R denote the work functions of the semiconductor and the electrolyte, respectively, V_H represents the potential drop across the Helmholtz layer, while $E_{f,n}$ and $E_{f,p}$ correspond to the quasi-Fermi levels of electrons and holes.

challenge. Notably, under Air Mass 1.5 Global (AM 1.5G) irradiation, a SC photoelectrode with a band gap 1.8 eV could achieve a photocurrent density of 19.7 mA cm^{-2} and an estimated theoretical maximum STH value of 24.2%. Of course, an increase in the bandgap value inevitably narrows the spectral absorption range, which generally results in reduced solar energy utilization and lower overall conversion efficiency.

2.1. Configuration of photoanodic water oxidation reaction and interfacial band bending

PEC hydrogen evolution is recognized as a promising strategy for converting abundant solar energy into storable chemical fuels, offering a pathway to alleviate the growing global energy and environmental challenges. SC photoabsorbers, serving as the core components, have long been at the centre of research interest. Actually, the OER phenomenon on illuminated rutile TiO$_2$ electrodes was first observed in 1968,[26] and shortly thereafter, Fujishima and Honda reported the pioneering demonstration of solar-driven electrochemical water splitting in 1972 using n-type TiO$_2$ as a photoanode, which is widely regarded as the inception of PEC water splitting.[27] Despite the excellent chemical stability of TiO$_2$, its wide bandgap (~3.2 eV) confines absorption to the ultraviolet (UV) region, thereby

restricting its solar energy utilization and conversion efficiency. Therefore, extensive efforts have been dedicated to designing narrow-bandgap photoactive semiconductors to enhance PEC performance. Building on these foundational studies, PEC water-splitting systems have advanced considerably, with recent reports achieving solar-to-hydrogen (STH) conversion efficiencies approaching 19%.[28]

Fig. 2a presents a schematic configuration of the representative PEC water-splitting system dominated by the photoanode. The setup typically includes an n-type semiconductor photoanode serving as the working electrode, a Pt counter electrode, and a simulated solar light source (AM 1.5G). As illustrated in Fig. 2b, the photoanodic OER proceeds through three main stages. (i) Photoexcitation: Upon illumination, the semiconductor absorbs photons with energies equal to or greater than its bandgap (hν ≥ Eg), leading to the generation of electron–hole pairs. The photoexcited electrons are promoted to the conduction band (CB), while the holes remain in the valence band (VB). (ii) Charge separation and transfer: Driven by band bending and aided by an applied bias, the photogenerated carriers are spatially separated. Electrons (majority carriers) migrate through the external circuit to the counter electrode, while holes (minority carriers) move toward the surface of the photoanode. However,

charge recombination may occur within the bulk semiconductor, at the surface, or across semiconductor/substrate and semiconductor/electrolyte interfaces, thereby diminishing the quantum efficiency.[29] Hence, strategies that enhance charge separation and injection efficiency are crucial for improving PEC performance. (iii) Surface redox reactions: At the counter electrode, the transferred electrons reduce protons (H^+) to hydrogen (H_2), while holes accumulated at the photoanode surface participate in the oxygen evolution reaction. Meanwhile, proton transport through the electrolyte completes the circuit, enabling the overall water-splitting reaction.

In a conventional PEC cell employing a single photoabsorber as the photoanode, an external bias is typically required to compensate for the overpotential and other energy losses. Unlike purely electrocatalytic water splitting, the photoanode replaces the catalytic anode for the OER, thereby driving the corresponding half-reaction under illumination. The incorporation of a photoanode allows partial or complete reduction of the external bias, with the compensated portion corresponding to the photovoltage (V_{Ph}) generated by the semiconductor absorber.[30] When V_{Ph} exceeds the combined potential of water oxidation ($E°(O_2/H_2O)$) and the associated overpotential requirements (~1.8 V), this PEC device can then achieve unassisted water-splitting process. To obtain sufficient photovoltage for spontaneous water splitting operation, advanced configurations such as photoanode–photocathode tandem cells or photoanode–photovoltaic (PV) tandem cells are often adopted. What's more, in some cases, anion or cation exchange membranes are introduced to separate the photoanode from the counter electrode, ensuring ionic conductivity while preventing product crossover. Additionally, conductive substrates such as silicon,[31] fluorine-doped tin oxide (FTO), or indium tin oxide (ITO)-coated glass are commonly utilized to support the deposition or growth of photoactive layers during photoanode fabrication.

Except for the SC photoanode module, the electrolyte also plays a crucial role in facilitating charge transport within the PEC system. In reality, electrolyte selection is not strictly defined, as the stability of different materials varies significantly across specific pH ranges. Noteworthily, in specific cases such as metal sulfides as photoanodes (e.g., CdS and TMDs), redox couples like H_2O_2, Na_2S, and Na_2SO_3 are generally introduced into the electrolyte as hole sacrificial agents, effectively replacing the photoanodic OER due to the lower oxidation potential of these species compared to water.[32, 33] The rapid harvesting of photogenerated holes by sacrificial agents helps to inhibit surface charge recombination, avoid back reactions, and protect the photoanode. Nevertheless, the use of sacrificial agents introduces additional costs. To enhance the economic feasibility, sacrificial organic compounds, including short-chain alcohols, carboxylic acids, and biomass-derived molecules, have been explored, offering the dual advantages of generating high-value-added chemicals alongside hydrogen production.[20, 34] Furthermore, this PEC reforming strategy can be applied for the treatment of organic-laden industrial wastewater, contributing to aquatic protection. Considering the mechanistic insights and operational principles of photoanode-based PEC systems

discussed above, it is evident that the primary factors and challenges for a practical PEC hydrogen production device include efficiency optimization and long-term photostability, which remain the focal points of current research.

In photoanode-dominated OER processes, band bending at the semiconductor/electrolyte interface is critical for facilitating the charge carrier separation and transport, making a thorough understanding of this phenomenon essential. When a SC photoanode comes into contact with an electrolyte, the difference between the SC's Fermi level (E_f) and the electrolyte redox potential drives a charge transfer until equilibrium is established, resulting in band bending within the semiconductor. Fig. 2c illustrates the band energetics at the photoanode/electrolyte interface under three conditions: before equilibration, after equilibration in the dark, and during quasi-static equilibration under steady-state illumination. Apparently, upon immersion of a typical n-type SC into the electrolyte, electrons flow across the interface until the E_f aligns with the redox potential of the electrolyte. This equilibration forms a depletion region, or space charge layer (W_{SCL}), in the semiconductor containing an excess of positive charges, which leads to upward band bending. Simultaneously, a narrow, anion-rich Helmholtz layer develops at the interface.[35] Under illumination, the generation of non-equilibrium electron and hole populations can be described using quasi-Fermi levels, which represent the electrochemical potentials of electrons and holes under steady-state light conditions. The resulting gradient of the quasi-Fermi levels induces a built-in electric field at the semiconductor surface,[36] producing a photovoltage (or open-circuit voltage, V_{OC}) that provides the powerful driving force for water oxidation. Experimentally, V_{OC} can be determined from the potential difference between the quasi-Fermi levels of electrons and holes under open-circuit conditions, while the maximum power output (P_{MAX}) can be estimated as the product of the short-circuit current (J_{SC}) and V_{OC}.

2.2. Charge separation and transfer behaviour within SC photoanodes

Photoanodic oxygen evolution is governed by several key processes, including photoexcitation, charge separation, and carrier transport. The efficiency of photoexcitation, which generates electron–hole pairs, is primarily determined by the intrinsic photoelectronic properties of the semiconductor, such as its bandgap and band-edge positions, as well as the spectral alignment of absorbed photons with the solar spectrum. Subsequent charge separation and transport critically influence the overall quantum efficiency. Ideally, radiative recombination within the bulk semiconductor is the only competing process, whereby emitted photons may be reabsorbed.[37] However, in practice, nonradiative pathways, including Shockley–Read–Hall (trap-assisted) recombination, Auger recombination, and other mechanisms, account for the majority of energy losses during the photo-to-current conversion.[38, 39] The schematic illustration of various charge carrier recombination pathways and relevant description are shown in Fig. S1. Furthermore, a mismatch between the diffusion length of photoexcited carriers, particularly minority carriers, and the light penetration depth also

ChemComm

exacerbates recombination, reducing PEC performance. For instance, in hematite, the hole diffusion length is reported to be only 2–4 nm, considerably shorter than the characteristic light penetration depth of ~46 nm at 450 nm illumination.[40, 41] As a result, most of photogenerated holes recombine before reaching the semiconductor surface to participate in the redox reaction. Consequently, only minority carriers generated within approximately one diffusion length of the depletion layer can be efficiently separated and drift toward the semiconductor/electrolyte interface. Under the assumption of negligible recombination in the depletion region, the instantaneous current of photogenerated minority carriers (J) can be estimated using the Gartner equation:[42, 43]

$$J = eI_0\left(1 - \frac{e^{-\alpha W}}{1+\alpha L_n}\right) \tag{5}$$

Here, I_0, e, α, W, and L_n denote the incident photon flux, elementary charge, absorption coefficient, width of the space charge layer, and minority carrier diffusion length, respectively. A larger diffusion length of minority carriers and an expanded space charge region are advantageous for achieving higher photocurrent densities. Additionally, an extended carrier lifetime (τ) and increased mobility contribute to a longer L_n, thereby enhancing charge separation efficiency.

Actually, charge carrier recombination occurs not only within the bulk semiconductor but also at the semiconductor surface or interfaces, where it manifests as a solid-state process.[44, 45] Even pristine semiconductors possess abundant surface electronic states, arising from defects such as structural imperfections and dangling bonds, regardless of whether the surface is in contact with a metal electrode or exposed to vacuum. These surface states are a primary source of charge recombination. Additional competing processes, including self-corrosion of the photoanode and side reactions, further impede surface charge transport, thereby reducing charge injection efficiency. Moreover, chemisorbed species, such as reactants, intermediates, or products formed during surface oxidation, can also serve as recombination centres, limiting the effective separation of photogenerated carriers.

The rational design of SC photoanodes with enhanced performance remains a central focus in advancing PEC technology for efficient solar hydrogen production. As outlined in the PEC water-splitting process, the primary factors limiting the performance of SC photoanodes are solar light absorption, charge separation, and charge injection efficiency. Over the past decades, numerous theoretical and experimental studies have explored a variety of modification strategies to address these limitations, including the development of narrow-bandgap photocatalysts, chemical doping or vacancy engineering,[46, 47] morphology design,[48] surface reconstruction,[49] noble metal coating,[50] heterojunction construction,[51-53] dye sensitization,[54] and co-catalyst deposition.[47] These approaches aim to broaden the light absorption range while minimizing both bulk and surface charge recombination, thereby improving quantum efficiency and overall PEC performanc.[55] However, individual strategies or materials rarely optimize all three aspects simultaneously; in practice, combining multiple modification

techniques is often necessary to achieve superior photoanode performance.

2.3. Performance parameters in photoanodic water oxidation reaction

Standardize parameters and efficiency measurements for photoanodic OER process provide quantitative information for comparison. The primary goal in designing photoanodes is to maximize the photocurrent density (J_{ph}) while minimizing the onset potential (V_{on}). Typically, the J_{ph} measured at 1.23 V_{RHE} is used as a benchmark to evaluate the PEC performance of a photoanode, with higher J_{ph} values indicating a greater number of photogenerated carriers participating in the water-splitting reaction. To provide a clearer understanding, the measured photocurrent density can be expressed through a simplified representation of the charge separation and transfer processes:

$$J_{ph}=J_{abs}\times\eta_{sep}\times\eta_{inj} \tag{6}$$

Herein, J_{abs} denotes the theoretical maximum photocurrent density determined by the SC's light absorption, η_{sep} corresponds to the bulk charge separation efficiency, reflecting the fraction of minority carriers that successfully reach the semiconductor/electrolyte interface rather than recombining in the bulk, and η_{inj} represents the surface charge injection efficiency, indicating the proportion of minority carriers that participate in the desired surface reaction instead of undergoing surface recombination. This framework allows for the experimental quantification of both bulk and surface carrier recombination processes.

In addition to bulk and surface charge recombination efficiencies, several other metrics are commonly used to evaluate the solar conversion efficiency, including the solar-to-hydrogen conversion efficiency (η_{STH}), incident photon-to-current efficiency (IPCE), absorbed photon-to-current efficiency (APCE), applied bias photon-to-current efficiency (ABPE), and Faradaic efficiency (FE). The corresponding calculation formulas for these parameters are provided below:

As a standard metric for evaluating and comparing PEC system performance, the solar-to-hydrogen conversion efficiency (η_{STH}) is calculated as the ratio of the chemical energy output to the total incident solar energy (AM 1.5G), as expressed below:

$$\eta_{STH}=\frac{(Total\ energy\ produced)}{(Total\ input\ energy)} = \left[\frac{r_{H_2}\times\Delta G}{P_{in}\times A}\right]_{AM1.5G} \tag{7}$$

Here, r_{H2}, ΔG, P_{in}, and A denote the hydrogen production rate (mol s^{-1}), the Gibbs free energy of water splitting (237 kJ mol^{-1}), the incident light intensity (100 mW cm^{-2}), and the illuminated area of the photoanode (cm^2), respectively. It is important to note that the η_{STH} metric is only valid for unbiased, two-electrode PEC configurations in the absence of sacrificial reagents.

The incident photon-to-current efficiency (IPCE) is a widely employed metric for assessing the photoelectric conversion performance of photoanodes at a specific illumination wavelength. It is defined as the ratio of the number of photoexcited electrons contributing to the photocurrent to the number of incident photons, as expressed by the following equation:

$$IPCE\ (\lambda) = \frac{The\ number\ of\ converted\ electrons}{incident\ photons} = \frac{(\frac{J(\lambda)}{e}) \times (\frac{hc}{\lambda})}{P(\lambda)} \times 100\% \quad (8)$$

In this expression, J (λ), e, h, c, λ, and P (λ) denote the photocurrent density at the specified incident wavelength (mA cm^{-2}), the elementary charge (1.602×10^{-19} C), Planck's constant (6.626×10^{-34} J s), the speed of light (3×10^8 m s^{-1}), the wavelength of the incident light (nm), and the corresponding light intensity (mW cm^{-2}), respectively.

The IPCE calculation described above is based on the total number of incident photons and does not account for optical losses due to reflection or transmission, which may introduce deviations in the measured efficiency. To address this limitation, the absorbed photon-to-current efficiency (APCE) is often used to more accurately evaluate the intrinsic quantum efficiency. APCE is defined as the ratio of photoexcited electrons contributing to the photocurrent to the number of photons actually absorbed by the photoanode, as expressed by the following equation:

$$APCE\ (\lambda) = \frac{IPCE\ (\lambda)}{\eta_{LHE}} \quad (9)$$

Here, η_{LHE} represents the light-harvesting efficiency of photoanodes, estimated from the corresponding absorption coefficient (α):

$$\eta_{LHE} = 1 - 10^{-\alpha} \quad (10)$$

In practical PEC measurements, a conventional three-electrode setup is commonly employed to evaluate photoanode performance. By excluding the contribution from externally applied bias, the applied bias photon-to-current efficiency (ABPE) can be determined using the following expression:

$$ABPE = \frac{J_{Ph} \times (1.23 - V_{bias})}{P_{light}} \times 100\% \quad (11)$$

Herein, J_{Ph} denotes the photocurrent density generated by the PEC device (mA cm^{-2}), V_{bias} represents the applied device bias, and P_{light} is the incident light intensity (100 mW cm^{-2}).

Faradaic efficiency (FE) is widely employed to verify whether the measured photocurrent density arises from water-splitting reactions rather than photoelectrode corrosion or other parasitic processes. It is defined as the ratio of the experimentally evolved gas quantity to the theoretical amount of gas calculated from the detected photocurrent density, as expressed by the following equation:

$$FE = \frac{Experimental\ O_2\ or\ H_2\ evolution}{Thoretical\ O_2\ or\ H_2\ evolution} = \frac{N}{(\frac{J_{Ph} \times A \times T}{Z \times F})} \times 100\% \quad (12)$$

In this expression, N denotes the experimentally measured gas amount determined by gas chromatography (GC, mmol), J_{Ph} is the photocurrent density (mA cm^{-2}), A represents the illuminated area of photoelectrode (cm^2), T is the durations of photoreaction (s), Z corresponds to the number of electrons required to generate one molecule of gas (2 for H_2, 4 for O_2), and F is the Faraday constant (96 485.33 C mol^{-1}).

Among the various efficiency metrics, η_{STH} is regarded as the most reliable parameter for rigorously benchmarking PEC water-splitting devices. Nonetheless, auxiliary metrics, such as ABPE
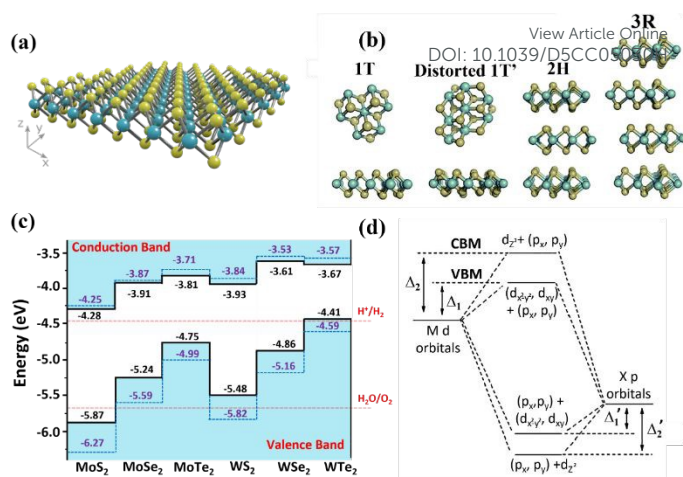

Fig. 3 (a) The typical crystal structure of monolayer TMDs, showing a transition metal plane (blue) is sandwiched between two chalcogen planes (yellow); (b) Different polymorphs or phases of single-layer TMDs: 1T, 1T′, 2H, and 3R-phases. Reproduced from Ref. 60 with permission. Copyright 2015 Royal Society of Chemistry. (c) Bandgap alignment of most representative monolayer TMDs used for photoanode fabrications; (d) Schematic illustration for the origin of conductance band maximum (CBM) and valance band maximum (VBM). Adapted from Ref. 62 with permission. Copyright 2013 AIP Publishing.

and IPCE, serve as valuable diagnostic tools, providing additional insight into the development and characterization of PEC materials.

3. Structure and advantages of TMDs-based heterostructure photoanodes

SC-based photoabsorbers, as the key component of PEC devices, have consistently been the focus of photoanode design. Upon the pioneering development of TiO$_2$ photoanodes in 1979, a variety of photoactive SC materials, e.g., CdS,[50] α-Fe$_2$O$_3$,[56] BiVO$_4$,[57] Ag$_3$PO$_4$,[58] Si,[59] etc., and relevant heterojunctions, have been explored and implemented for PEC water splitting, leading to significant advancements in device performance. However, their practical photoconversion efficiencies are still far from satisfactory. Fortunately, the emerging and investigation of low-dimensional TMDs injects renewed impetus into the construction of highly-performing photoanodes for PEC water splitting, due to their extraordinary physicochemical, photoelectronic, and catalytic properties.

In general, TMDs are composed of hexagonal layers in which a transition metal plane is sandwiched between two chalcogen planes, with an individual layer thickness of approximately 6–7 Å, as shown in Fig. 3a. The stacking arrangement of these layers dictates both the crystal structure and the resulting physicochemical properties of the materials.[11] The most prevalent polymorphs include the 1T, 1T′, 2H, and 3R phases, corresponding to trigonal, distorted trigonal (octahedral), hexagonal, and rhombohedral structures, respectively (Fig. 3b).[60] These structural configurations arise from the electronic interactions between the valence d-orbitals of the transition metal atoms and the p-orbitals of the chalcogen atoms.[61] Specifically, the 1T and 1T′ polymorphs adopt octahedral and distorted octahedral coordination, respectively, and generally exhibit metallic behavior characterized by high electrical conductivity.

In contrast, the 2H phase, which contains two hexagonal layers per unit cell, and the 3R phase, comprising three rhombohedral layers, typically display semiconducting properties with bulk bandgaps ranging from 0.3 to 2.0 eV. The band alignment of the most representative monolayer TMDs used for photoanode fabrications, and the origins of the conduction band minimum and valence band maximum for these phases are illustrated in Fig. 3c, d.[62] Overall, the electronic and optical characteristics of TMDs are strongly governed by the coordination geometry of the transition metal centers and their d-electron occupancy.[63]

As typical layered materials, a defining characteristic of TMDs is that their bulk crystals are composed of multiple stacked layers held together by weak van der Waals (vdW) interactions. These layers can be exfoliated into mono- or few-layer structures through approaches such as mechanical exfoliation, liquid-phase exfoliation, and ball milling method, thereby increasing the density of catalytically accessible sites. The intrinsically large surface-to-volume ratio of 2D TMDs provides abundant photoreactive centers for light harvesting and interfacial reactions. Among them, Molybdenum (Mo)-based TMDs, particularly MoS_2, have attracted considerable interest as promising alternatives to platinum (Pt) for HER catalysis, owing to their comparable catalytic activity and superior stability. While numerous studies indicate that the edge sites are generally more catalytically active than the basal planes, plenty of efforts are thus employed to expose more active edge sites and activate basal planes through surface modification, phase or defecting engineering.[64-67] Next, TMDs possess superior solar absorption capability and their bandgaps can be easily modulated via thickness variation, chemical doping, and strain engineering.[68, 69] Due to their narrow bandgaps and matched band position with redox potentials of water, TMDs become an ideal photosensitizer to optimize the over light harvesting efficiency. In addition, 2D TMDs materials also exhibits several other distinct advantages, including high light transmission with enhanced photon-matter interactions, enormous charge mobility (~200 cm^2 V^{-1} s^{-1} for MoS_2), and short carrier diffusion pathway, which is beneficial for yielding electron-hole pairs and fast charge transport across materials.[70] More importantly, Van der Waals interactions allow TMDs materials to be assembled onto diverse substrates or stacked into multilayers without inducing lattice mismatch or atomic interdiffusion, unlike covalently bonded materials that often cause mechanical strain and structural distortion.[17] All the above structural features and property superiorities offer TMDs materials potential and flexibility to incorporate with other SCs for Van der Waals heterojunctions fabrication.

Among the family of TMDs, Molybdenum/Tungsten disulfides, like MoS_2 and WS_2, have obtained much more attention and serve as the most common photoanode materials. However, since TMD nanomaterials are susceptible to desulfurization or corrosion under alkaline conditions and high overpotentials, their long-term stability and durability remain a critical limitation for OER applications in PEC water splitting. To address this issue, recent research has shifted toward employing TMDs as cocatalysts or photosensitizers in PEC-OER systems, rather than as the primary OER photocatalysts. Ingeniously assembling low-dimensional TMDs onto other photoactive semiconductor scaffolds to construct heterojunctions is the most prevalent and useful method to optimize PEC performance. Their synergistic effects and formed built-in electrical field within interfacial junctions can effectively improve the overall light absorption, promote charge separation and transfer, increase surface reaction sites, and enhance photocorrosion resistance. The positive roles of TMDs in various heterojunction architectures can be summarized as photosensitizers, electron transporting mediators, passivation layers, cocatalysts, and protective layers. The relevant synthetic routes, recent advancements, and our contributions in designing and manufacturing TMDs-based heterostructure photoanodes are reviewed below.

4. Design and fabrication of TMDs-based heterostructure photoanodes

A heterojunction is established when two or more semiconductors are brought into direct contact, creating an interface that facilitates efficient charge transfer between the constituent materials. Elaborately integrating low-dimensional TMDs with other primary semiconductor photoabsorbers to form heterojunctions can tackle the weakness of each component well, synergistically devoting to the overall PEC performance. Generally speaking, the fabrication of heterojunctions typically requires semiconductors with compatible crystal structures, lattice parameters, and thermal expansion coefficients. Lattice mismatch at the interface can lead to weak interfacial bonding and the formation of defects, which hinder efficient charge transfer.[71] Therefore, diverse synthetic methods and preparation routes are employed to improve the quality of heterojunctions with intimate interfacial contact and high-speed charge transport channel between semiconductors.

4.1. General synthetic strategies

Unlike other 2D nanomaterials, low-dimensional TMDs with different microstructures and morphologies, such as 2D few/mono layered thin films, triangular nanoflakes, nanosheet clusters, or quantum dots, can be synthesized by a wide variety of approaches, including, mechanical/liquid-phase exfoliation,[72, 73] chemical vapor deposition (CVD),[74] solvo/hydrothermal synthesis,[75, 76] etc. The versatility of TMDs synthesis gives rise to a wide range of possible architectures for TMDs-based heterostructures, whether via in situ assembly or ex situ incorporation. In summary, fabrication strategies for TMDs-based heterostructure photoanodes can be broadly categorized into two approaches: top-down and bottom-up methods, shown in Fig. 4a.

4.1.1. Top-down methods. Top-down methods mean the pre-prepared TMDs are directly physically deposited on the surface of other semiconductor scaffolds without any growth or chemical reaction process, represented by spin-coating, drop-casting, dip-coating, RF magnetron sputtering, solution-assisted coating, liquid−liquid self-assembled method, and electrostatic assembly. These approaches are well-suited for flexible substrates and can be carried out under ambient or room-temperature conditions.
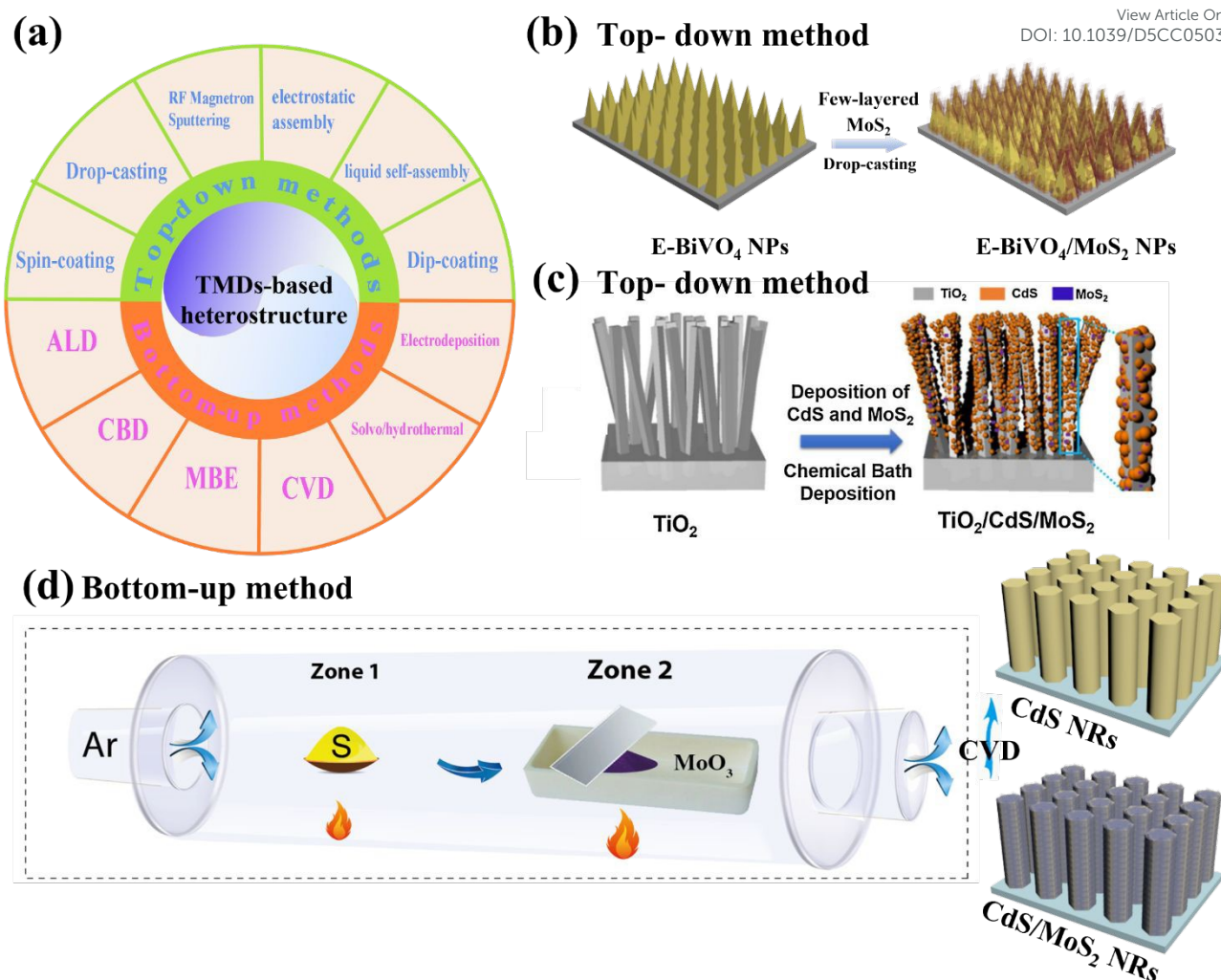
Fig. 4 (a) The general synthetic strategies for TMDs-based heterostructure photoanodes categorized by: top-down and bottom-up methods; (b, c) Representative top-down methods of drop-casting and CBD; Reprinted from Ref. 77 and 78 with permission. Copyright 2023 Elsevier and Copyright 2019 Elsevier. (d) Representative bottom-up route of CVD. Reprinted from Ref. 32 with permission. Copyright 2023 Elsevier.

For example, Siaj's group successfully fabricated a highly-oriented E-BiVO$_4$/MoS$_2$ heterojunction photoanode via directly drop-casting exfoliated few-layered MoS$_2$ nanosheets on electrochemically-treated BiVO$_4$ nanopyramids, followed by further heat treatment at 400°C for 1h under Ar atmosphere, as shown in Fig. 4b.[77] In addition, Jiang et al. demonstrated the fabrication of a heterojunction photoanode comprising 2D MoS$_2$ nanosheet-modified 1D TiO$_2$ nanorods (NRs) integrated with 0D CdS nanocrystals.[78] This architecture was realized via in-situ chemical bath deposition, achieved by immersing the TiO$_2$ NR film into a CdS precursor solution containing exfoliated MoS$_2$ nanosheets, as illustrated in Fig. 4c. As mentioned above, TMDs are generally employed as cocatalysts rather than primary photoactive materials because of their limited intrinsic photoactivity. Consequently, top-down methods typically start with high-purity exfoliated 2D TMDs, which can be readily incorporated onto semiconductor scaffolds without requiring in situ growth. This approach offers clear advantages in terms of cost-effectiveness and scalability, making it particularly suitable for large-area deposition and roll-to-roll manufacturing. However, the thickness, lateral size, and uniformity of exfoliated

TMD flakes are inherently difficult to regulate, often resulting in limited control over flake distribution, orientation, and interfacial junction quality within the assembled heterostructures. Such limitations may lead to flake agglomeration, structural heterogeneity, and increased interfacial defect density. Moreover, many top-down processed films require subsequent high-temperature annealing to improve interfacial adhesion or crystallinity, which may unintentionally introduce impurity states, alter energy-level alignment, or even induce undesirable phase transitions.

4.1.2. Bottom-up methods. Conversely, the bottom-up approach assembles materials in an atom-by-atom manner from molecular or ionic precursors, enabling precise control over size and dimensionality. In this strategy, TMDs precursors are typically introduced into a reaction chamber together with other semiconductor frameworks deposited on a substrate, wherein TMDs will directly grow on the surface of semiconductor scaffold to push the formation of TMDs-based heterojunctions. Bottom-up methods are majorly involved in atomic layer deposition (ALD),[33] chemical vapor deposition (CVD),[32] solvo/hydrothermal deposition,[79, 80] chemical bath deposition

(CBD),[81] electrodeposition,[82] and molecular beam epitaxy (MBE).[83] These approaches are convenient and amenable to large-scale production, though it is often limited by its time-intensive and costly nature. Among these methods, the CVD method represents one of the most effective approaches for synthesizing high-quality 2D TMDs with precisely controlled thickness, which can be grown either with or without pre-depositing a transition metal precursor onto the target substrate. As illustrated in Fig. 4d, Siaj's group reported the preparation of a core-shell CdS/MoS_2 heterojunction photoanode for PEC hydrogen evolution via the facile CVD method, where a continuous crystalline MoS_2 nanosheet layer was directly grown on one-dimensional, vertically aligned CdS nanorods via a plane-to-plane stacking configuration.[32] During this CVD process, sulfur powder as the S source was put in the upstream (Zone Ⅰ) and molybdenum trioxide as the Mo source was placed at the downstream heating zone (Zone Ⅱ). By adjusting the vertical spacing between the CdS substrate and the Mo source, the controlled growth of MoS_2 ultrathin films ranging from monolayers to a few layers was achieved. As demonstrated, vapor-phase techniques, such as CVD, ALD, and MBE, provide exceptional control over crystallinity, thickness, and interfacial architecture, enabling the conformal fabrication of high-quality and well-defined heterojunctions. However, these advantages come with notable drawbacks. Such methods typically require high temperatures, vacuum environments, and sophisticated instrumentation, which significantly increase cost and technical complexity. Moreover, because TMD layers are grown directly on the underlying semiconductor scaffolds, the surface properties of the substrate, including roughness, surface states, and adhesion, strongly affect the nucleation behaviour, film uniformity, and ultimately the PEC performance. Consequently, vapor-phase methods are more commonly employed for producing large-area TMD thin films for applications such as solar cells, field-effect transistors, photodetectors, gas sensors, and OLEDs, rather than for constructing TMD-based photoanodes.[13, 84] In contrast, solution-based bottom-up methods, including solvo/hydrothermal deposition and chemical bath deposition (CBD), offer greater practicality for large-scale fabrication. These methods can be conducted at relatively low reaction temperatures and are cost-effective in terms of raw materials, equipment, and energy consumption. Additionally, these methods enable the synthesis of TMD nanostructures with high purity, tunable morphology, and strong substrate affinity, which facilitates the formation of intimate and coherent heterointerfaces during in situ growth. Taken together, these advantages make solution-based bottom-up approaches the most commonly adopted strategies for preparing TMD-based heterostructure photoanodes in current PEC research.

4.2. Band engineering for optimized photoexcition separation and injection

Except for the selection of materials and synthetic methods, another consideration is involved in the heterostructure types. In semiconductor-based photoanodes, photoexcited charge carriers often undergo recombination before reaching to the photoelectrode surface and participating in photoreaction. To promote the efficient charge separation and injection, heterojunction fabrication by the incorporation of TMDs as the hole transporting layers (HTL) is essential. To direct charge migration effectively, it is essential to establish well-matched band alignment with favourable electron transfer energetics. Generally speaking, based on the distinct charge transfer mechanism, the TMDs-based heterojunctions can be categorized into the following configurations: conventional heterostructures (Types-I and II), Z-scheme architectures, p–n junctions, and Schottky junctions. A detailed discussion of these classifications is provided in the following section. Meanwhile, a comprehensive summary and comparison of their PEC performances and photoconversion efficiencies are presented in Table 1.

4.2.1. Types I heterostructure. In a typical type I heterostructure with straddling bandgap junctions shown in Fig. 5a, the CB and VB positions of semiconductor scaffolds are generally higher and lower than those of semiconductor (SC) B. Both photoexcited electrons and holes are transferred from the semiconductor scaffold to SC B without any external bias, which largely suppresses the charge recombination process within the host semiconductor and improves the overall quantum efficiency. Low-dimensional TMDs feature large specific surface areas and relatively low VB positions, enabling them to act as efficient hole-acceptor and transporter layers. In the formation of TMDs-based type-I heterojunctions, these characteristics facilitate charge separation while offering abundant reactive active sites, thereby boosting PEC water splitting. For example, Siaj's group reported a novel core/shell CdS/MoS_2 type-I heterostructure photoanode fabricated via a facile CVD process, where a continuous crystalline MoS_2 nanosheet layer was directly grown on the surface of CdS with the formation of an intimate interface junction (Fig. 5b).[32] UV–vis-NIR diffuse reflectance spectroscopy (DRS) and photoluminescence spectroscopy (PL) analysis suggest that the coated MoS_2 shell can not only act as the photo absorption booster to broaden the spectrum absorption range of CdS, but also function as the surface passivator of trap states to suppress its bulk charge carrier recombination. As shown in Fig. S2a, the absorption edge of the CdS/MoS_2-3L NRs obviously red-shifts to the longer wavelength of around 534 nm compared to the pristine CdS, implying more production of photogenerated charge carrier. Fig. S2b demonstrates significantly quenched PL intensities on both band and trap-state emission peaks of CdS/MoS_2, verifying a reduced recombination and trapping process of photoexcited electron-hole pairs in this system. Furthermore, Mott-Schottky plots, electrochemical impedance spectroscopy (EIS), and the time-resolved photoluminescence (TRPL) curves manifested that introducing dual-phase MoS_2 as a heterojunction can effectively weaken the bulk charge transfer resistance of CdS, prolong the electron lifetimes, and achieve the rapid spatial separation of photogenerated charge carriers across the bulk and interface. The quantitative calculation, shown in Fig. S2c, reveals that the resulting CdS/MoS_2-3L NRs possesses a remarkably improved charge separation efficiency from 10.3% to 25.4% at 1 V vs RHE, compared to the bare CdS. As a result, the optimum CdS/MoS_2 heterojunction photoanode, featuring a
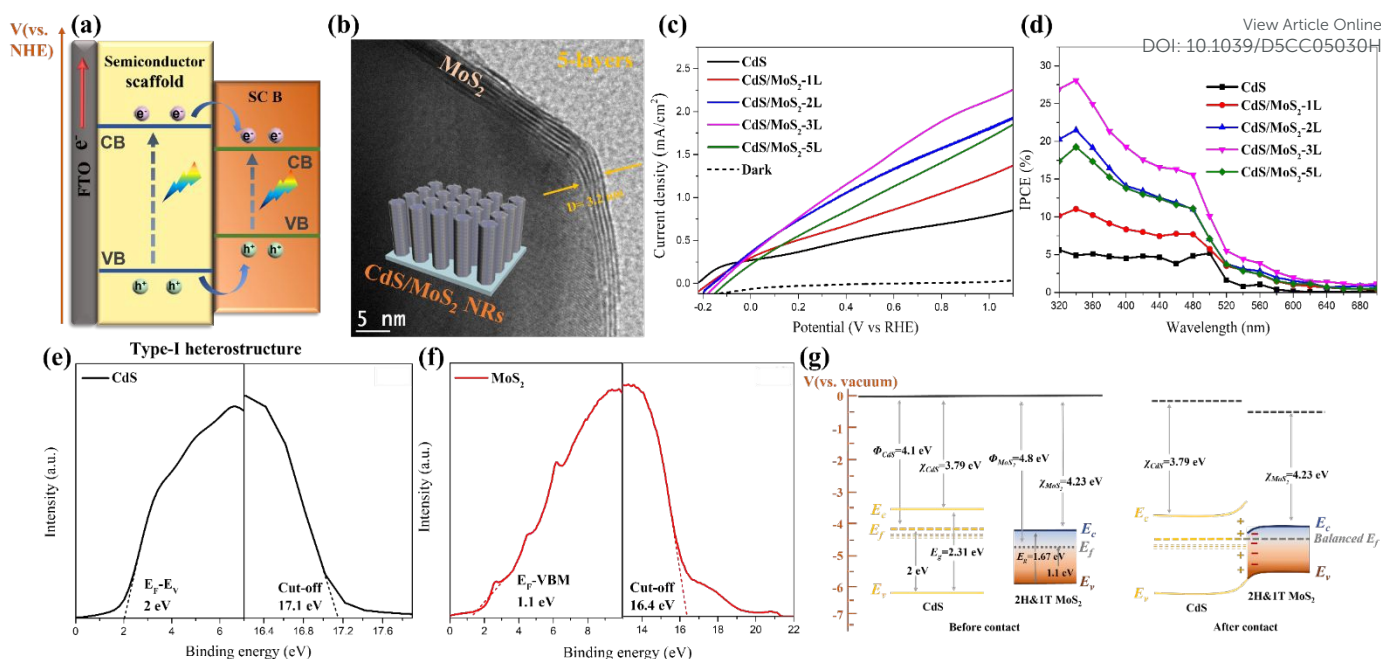
Fig. 5 (a) Type-I heterostructure with straddling bandgap alignment. (b) HRTEM image of the CdS/MoS₂ nanorod with distinct core-shell structural feature as the insert; (c) LSV curves measured at Na₂SO₃/Na₂S mixture using a three-electrode setup and (d) IPCE plots of the pristine CdS and CdS/MoS₂ heterojunction photoanodes; (e, f) UPS spectra of the bare CdS and MoS₂ nanoflakes. $E_{Cut-off}$ denotes the spectrum edge of secondary electrons. E_F-E_V means the valance band energies relative to the Fermi levels. (g) The resulting Type-I energy band alignment of MoS₂ and CdS before and after interface contact at thermal equilibrium in darkness. Φ, E_f, E_c, and E_v represent work function, Fermi level, conduction band edge, and valance band edge, respectively. Reprinted from Ref. 32 with permission. Copyright 2023 Elsevier.

three-layer MoS₂ coating, delivers the maximum photocurrent density of 2.14 mA cm⁻² at 1 V_{RHE} and higher photoconversion efficiency within the entire photoexcitation region (Fig. 5c and d), achieving more than a two-fold increment relative to pristine CdS. Consequently, the detailed energy band structures were revealed by the ultraviolet photoelectron spectroscopy (UPS). As shown in Fig. 5 e and f, the Fermi levels (E_f) of the CdS and MoS₂ nanoflakes are estimated to be 4.1 eV and 4.8 eV, respectively, through subtracting the secondary electron cut-off energies from the excitation energy of 21.2 eV. The valance band energies relative to the Fermi levels are recorded to be 6.1 eV and 5.9 eV. Combined with their bandgap values read from Tauc plots (Fig. S2d), the conduction band edges (Ec) and resulting energy band alignment of both semiconductors are identified. As displayed in Fig. 5g, when CdS nanorods and MoS₂ shells establish intimate interfacial contact, the mismatch in their energy band structures induces charge rectification at the junction. Electrons are rapidly transferred from the CdS core to the MoS₂ shell, leading to Fermi level equilibration accompanied by band bending and the formation of a space charge region. Consequently, a typical Type-I heterojunction is established. Fig. S2e presents the plausible electron–hole transfer process, wherein photogenerated holes in the valence band of CdS are directionally transferred to the MoS₂ valence band, thereby effectively mitigating carrier recombination, accounting for their enhanced PEC hydrogen evolution performance. Notably, the accelerated hole extraction from CdS and the redistribution of surface oxidation sites endow the CdS/MoS₂ heterostructure with superior corrosion resistance and enhanced photostability.

Jang et al. demonstrated the formation of a Type I heterojunction photoanode, composed of 2D MoS₂ nanosheet modified 1D TiO₂ NRs/0D CdS nanocrystals prepared by the all solution process

(Fig. S3a), for PEC hydrogen evolution application.[78] Compared to the pristine TiO₂/CdS, this heterojunction photoanode exhibits a significantly higher photocurrent density of 3.25 mA/cm² at 0.9 V_{RHE} and IPCE enhancement. Through a series of electrochemical (EC), PEC, and TRPL analysis, it is concluded that the introduction of MoS₂ as a Type I heterojunction greatly facilitates the interfacial hole capturing, extends the electron lifetime, and optimizes the charge transfer efficiency, thereby resulting in this PEC enhancement. The straddling/staggered energy band alignment and Type Ⅱ/Type I charge transport pathway is displayed in Fig. S3b. Note that photoexcited electrons are injected into TiO₂ from CdS under thermodynamic driving forces due to the formation of Type Ⅱ heterojunction. The higher VB edge of MoS₂ facilitates the efficient transfer of photogenerated holes from CdS VB to MoS₂, leading to the reduced charge recombination loss. Shen. et al. also synthesized an efficient 2D-2D type I heterojunction photoanode (Fig. S3c and d) through decorating 2D COF with MoS₂ for PEC water oxidation.[85] The CB and VB values of triazine-based COF and MoS₂ are determined using Mott-Schottky measurements and VB XPS spectra analysis, confirming the formation of straddling energy band alignment. The fabrication of MoS₂/TTZ-COF Type I heterojunction can not only accelerate charge separation and transfer, but also enhance water oxidation kinetics, thus leading to the improved photocurrent density (Fig. S3e), negatively-shifted onset potential, and higher IPCE values. Although these previous studies highlight the effectiveness of Type-I heterojunctions in enhancing PEC performance, the accumulation of photoexcited electrons and holes within the same semiconductor in the absence of an external bias often leads to severe exciton recombination and reduced quantum
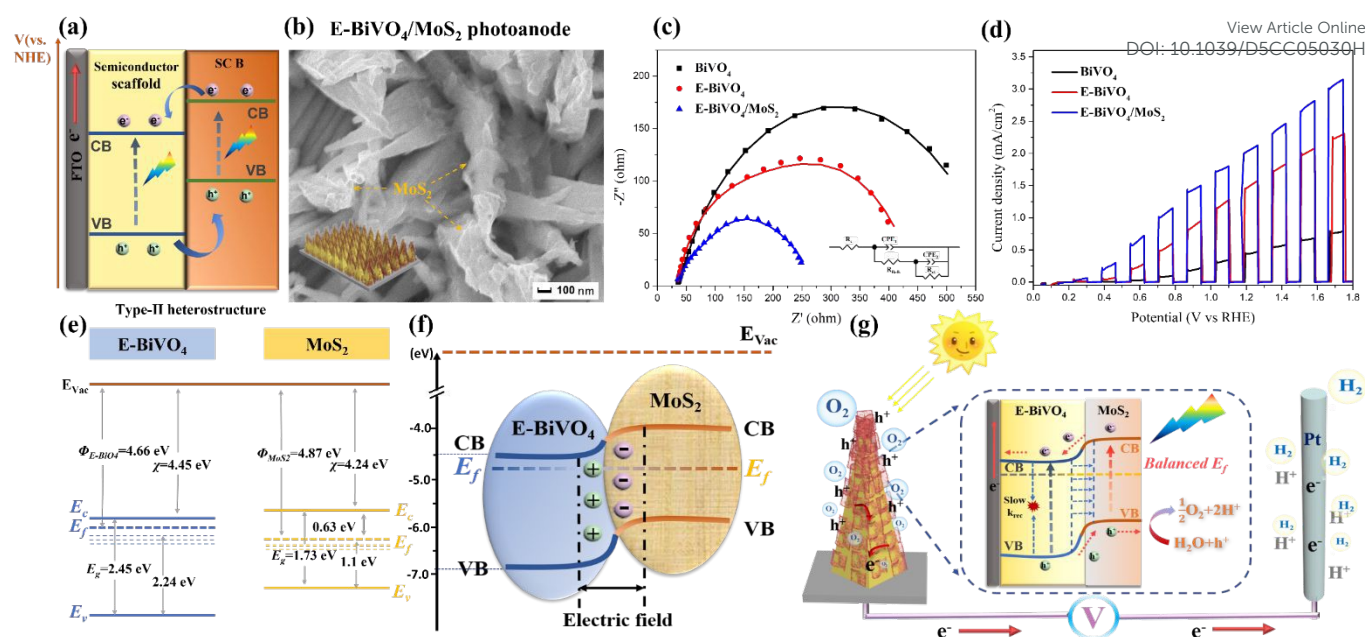
Journal Name

Fig. 6 (a) Type II heterostructure with staggered bandgap junctions; (b) Top-view SEM image of E-BiVO$_4$/MoS$_2$ nanopyramid arrays with the corresponding structural diagram as the inset; (c) Nyquist plots under sunlight irradiation and (d) Chopped LSV curves over the pristine BiVO$_4$, E-BiVO$_4$, and E-BiVO$_4$/MoS$_2$ heterojunction photoanode measured at a mixture of 0.5 M Na$_2$SO$_4$ and 0.1 M PBS solution with a typical three-electrode setup; (e) The detailed energy band information of E-BiVO$_4$ and MoS$_2$ nanosheets; Φ, E$_f$, E$_c$, and E$_v$ represent work function, Fermi level, conduction band edge, and valance band edge, respectively; (f) The energy band alignment at E-BiVO$_4$/MoS$_2$ heterojunction interface and (g) the possible Type II charge transfer pathway over this heterojunction photoanode system. Reprinted from Ref. 77 with permission. Copyright 2023 Elsevier.

efficiency. Moreover, the interfacial transfer of holes from a higher to a lower VBM potential inevitably leads to a pronounced reduction in oxidation capability. These constraints explain the relatively limited number of reports on TMDs-based Type-I heterojunctions in recent years, which greatly limit its further advancements.

4.2.2. Types II heterostructure. In Types II heterostructures with staggered bandgap junctions (Fig. 6a), both CB and VB of SC scaffolds should be higher than those of SC B. In contrast to Type-I heterostructures, Type-II heterojunctions feature an intrinsic energy gradient that directs photogenerated electrons and holes toward opposite semiconductors, promoting spatial separation and reducing charge recombination. Consequently, constructing Type-II heterojunctions by integrating wide- and narrow-bandgap SCs is widely regarded as an effective strategy to enhance both the overall quantum yield and PEC efficiency.

In recent years, a variety of TMDs-based Type-II heterostructures with diverse nanoarchitectures have been investigated, including stacked planar films, core–shell nanorods, and quantum-dot-decorated nanowires. Compared with single-component photoabsorbers, these TMDs-based Type-II heterostructure photoanodes, including MoS$_2$@BL-BiVO$_4$,[81] E-BiVO$_4$/MoS$_2$,[77] W:α-Fe$_2$O$_3$/MoS$_2$,[86] MoS$_2$/WS$_2$,[87] TiO$_2$/MoS$_2$-rGO/Zn-CuInS$_2$,[88] MoS$_2$/WO$_3$,[89-91] α-Fe$_2$O$_3$/BiVO$_4$/MoS$_2$,[92] ZnO/MoS$_2$,[93-96] MoS$_2$/In$_2$S$_3$,[97] MoS$_2$@(010)-BiVO$_4$,[82] F-Fe$_2$O$_{3-x}$/MoS$_2$,[98] MoS$_2$/ZnO/graphene/NF,[99] TiO$_{2-x}$-MoS$_2$,[100] Au/TiO$_2$/MoS$_2$,[101] MoS$_2$/GQD/ZnO,[102] W/WO$_3$/WS$_2$,[103] Fe$_2$O$_3$/WS$_2$,[104] CdS/WS$_2$,[105] WS$_2$/TiO$_2$,[106] WO$_3$@WS$_2$,[107] etc., all demonstrated higher PEC performance and solar conversion efficiencies. Taking one of our works as an example, an innovative highly-oriented E-BiVO$_4$/MoS$_2$ Type-II heterojunction photoanode

was prepared through drop-casting exfoliated few-layered MoS$_2$ nanosheets on oxygen-vacancy-rich BiVO$_4$ nanopyramid arrays (Fig. 6b).[77] As shown in Fig. 6c and S4a, EIS analysis and efficiency calculation provide the power evidence that encapsulating MoS$_2$ as a Type-II heterojunction with the built-in electrical field can greatly boost the hole extraction from E-BiVO$_4$ host and enhance the overall charge injection efficiency. Simultaneously, the electrochemical surface-active areas (ECSA, Fig. S4b) and DRS analysis indicate the improved surface reaction action sites and light harvesting after MoS$_2$ decoration. Accordingly, the engineered E-BiVO$_4$/MoS$_2$ Type-II heterojunction photoanode delivers the optimum photocurrent density of 2.11 mA cm^{-2} at 1.23 V$_{RHE}$ (Fig. 6d) and IPCE value of 40.6%, representing enhancements of approximately 4.6- and 4.9-fold over pristine BiVO$_4$, together with improved OER kinetics and superior photostability. Based on the relevant Tauc plots and UPS analysis, the detailed energy band distribution of E-BiVO$_4$ and MoS$_2$, and the formation of heterojunction interface with staggered bandgap configuration are confirmed, shown in Fig. 6e and f. Upon the direct contact of E-BiVO$_4$ and MoS$_2$, a charge rectification process will occur to achieve the thermodynamic equilibrium of Fermi level. The higher work function of E-BiVO$_4$ (4.66 eV) can induce the rapid electron transfer from E-BiVO$_4$ to MoS$_2$ shell, forming an upward band bending near E-BiVO$_4$ interface and built-in electric field. Thus, a plausible Type-II charge transfer route and operation mechanism are proposed. As displayed in Fig. 6g, under solar illumination, both semiconductors can be photoexcited to generate charge carriers due to their suitable bandgaps. Electrochemically induced oxygen vacancies help suppress bulk charge carrier recombination (K$_{rec}$), facilitating the release and migration of photogenerated holes to the photoanode
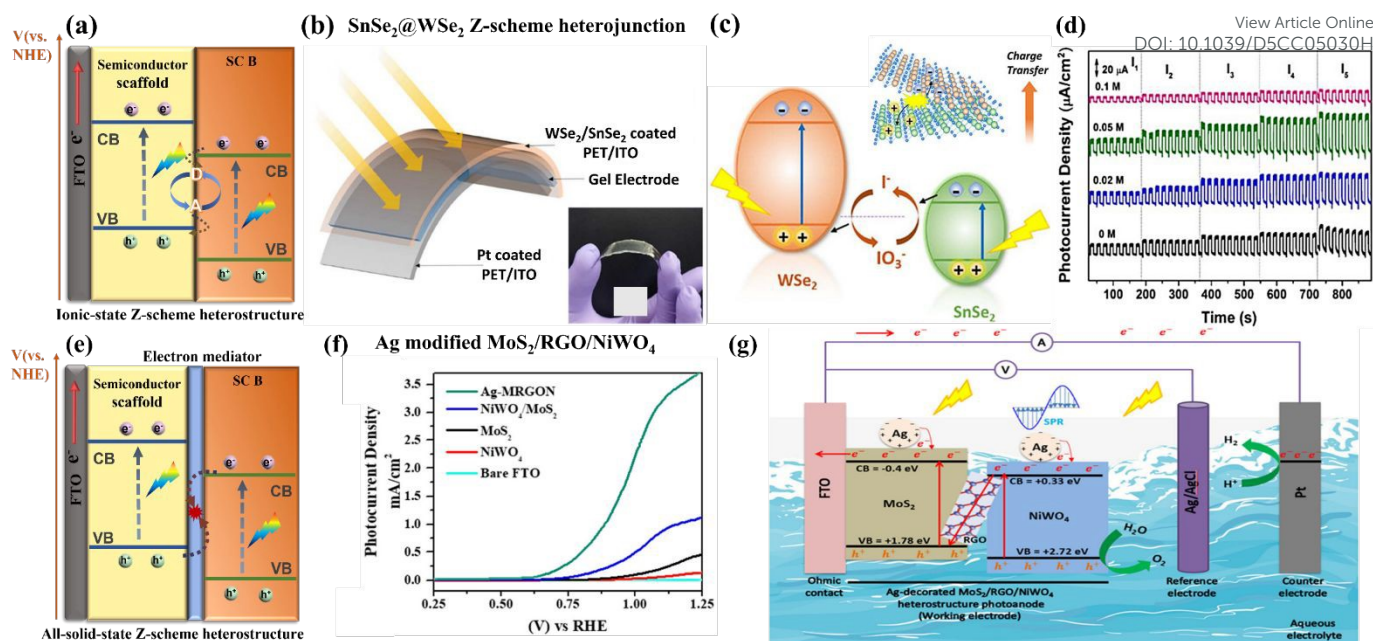
Fig. 7 (a) Schematic illustration of ionic state Z-scheme heterostructure; (b) Schematic illustration of the prepared flexible SnSe₂/WSe₂ photodetector with the real digital image as the inset; (c) The possible charge transfer model and (d) on/off photoresponse switching behaviour over SnSe₂/WSe₂ ionic state Z-scheme heterostructure photoanode system in 0.5 M KOH with different molar concentrations of KI; Herein, the IO₃⁻/I⁻ redox couple accepts the photoexcited electrons from the CB of SnSe₂ and holes from VB of WSe₂, thus promoting the efficient spatial charge separation across the heterojunction. Reprinted from Ref. 108 with permission. Copyright 2021 American Chemical Society. (e) All-solid-state Z-scheme heterostructure model. (f) LSV curves measured in 0.5 M Na₂SO₄ with a standard three-electrode configuration and (g) the proposed charge transfer pathway over the Ag-MRGON all-solid-state Z-scheme photoanode system. The rGO conductive matrix facilitates the recombination between NiWO₄ CB electrons and MoS₂ VB holes, thereby optimizing the Z-scheme charge-transfer pathway. Reprinted from Ref. 109 with permission. Copyright 2020 American Chemical Society.

surface. Further modification with MoS_2 nanosheets to construct a Type-II heterojunction establishes unidirectional charge-transfer pathways, facilitating the rapid extraction of surface-accumulated holes from E-$BiVO_4$. These holes are driven into the MoS_2 valence band by the synergistic effects of the built-in electric field and electrostatic interactions, then participating in the water oxidation reaction. Meanwhile, under an applied bias, photoexcited electrons in the CB of MoS_2 migrate toward the CB of E-$BiVO_4$ and flow together to the Pt electrode for hydrogen evolution. The well-separated photogenerated electron-hole pairs finally contributes to the enhanced photoresponse.

Roy's group reported the fabrication of a Fe_2O_3/WS_2 Type-II heterojunction photoanode (Fig. S5a) through drop-casting WS_2 nanosheets on Fe_2O_3 nanoflake arrays, followed by annealing in a N_2 atmosphere.[104] This heterojunction presents significantly improved optical absorption, photoresponse, ABPE and IPCE values, and obtains a synergistic photocurrent density of 0.52 mA cm⁻² at 1.3 V_{RHE}, 2.23 times higher than the pristine Fe_2O_3. The staggered energy band alignment (Fig. S5c) and charge transfer mechanism are confirmed by the DFT method and XPS valence band spectroscopy. The Density of States plots reveal both higher CBM and VBM positions of WS_2 than those of Fe_2O_3, conforming to the type-II energy band distribution. Bader charge analysis with charge density difference plots, presented in Fig. S5b, further verifies the occurrence of charge redistribution with a net charge flow of $4.8×10^{-4}$ e/interfacial unit from WS_2 to the Fe_2O_3 side. This charge transfer results in the formation of charge accumulation/depletion layer and a weak built-in electric field at heterogeneous interface, helping the rapid charge separation and hindering charge carrier

recombination. Lee et al. prepared a unique W:$α$-Fe_2O_3/MoS_2 heterojunction photoanode through directly drop-casting exfoliated MoS_2 nanosheets on W-doped $α$-Fe_2O_3 surface (Fig. S5d).[86] The optimum 0.5W: $α$-Fe_2O_3/MoS_2 photoanode achieves the highest photocurrent density of 1.83 mA cm⁻², IPCE value of 37%, and ABPE value of 26%, which are 26, 5.2, and 13 times higher than those of pure $α$-Fe_2O_3, respectively. The UPS spectra are used to analyse the relevant energy band information, wherein the VBM positions of W:$α$-Fe_2O_3 and MoS_2 are determined to be 6.49 and 5.27 eV through subtracting the UPS spectrum width from the excitation energy. Their work functions are estimated to be 5.05 and 4.34 eV. When W:$α$-Fe_2O_3 and MoS_2 are in contact, the Type-II heterojunction with band bending near the interface is established, as shown in Fig. S5e. The collaborative approach of heterojunction fabrication and atomic doping co-devotes to increasing carrier density, reducing the space charge layer, and decreasing flat band potential, thereby resulting in this remarkably PEC performance enhancement. However, the Type-II heterostructure shares a similar drawback with the Type I junction, where the charge carrier separation certainly brings a decrease in redox capability. Besides, the presence of electrostatic repulsion will also lead to a charge barrier and loss. Therefore, more types of heterostructures are developed for optimizing charge separation.

4.2.3. Z-scheme heterostructures. In recent years, Z-scheme heterojunctions have garnered significant attention because of their distinct advantages. Different from conventional Type-I or Type-II heterojunctions, which separate photoexcited electrons and holes at the expense of their redox potentials, Z-scheme heterojunctions enhance charge carrier dynamics while
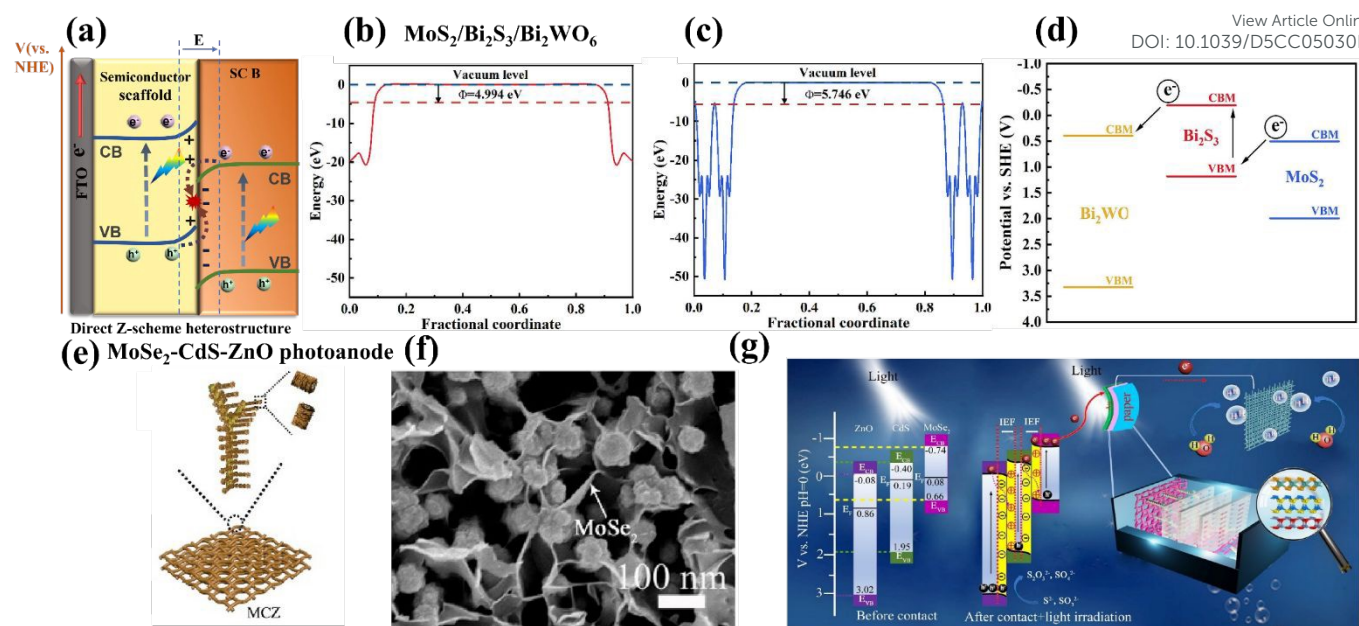
Fig. 8 (a) Schematic illustration of direct Z-scheme heterostructure; (b, c) DFT-based work functions of Bi_2S_3 and MoS_2, and (d) photoexcited charge transfer direction over the reported type II/Z-scheme $MoS_2/Bi_2S_3/Bi_2WO_6$ heterojunction photoanode; Herein, the photogenerated electrons in CBM of MoS_2 trend to recombine with the VBM holes of Bi_2S_3, forming direct Z-scheme charge transfer pathway. The synergistic effect of type II heterojunction further drives the remaining CBM electrons of Bi_2S_3 to Bi_2WO_4 for PEC H_2 evolution. Reprinted from Ref. 110 with permission. Copyright 2025 Elsevier. (e) Fabrication process and (f) SEM image of $MoSe_2$-CdS-ZnO flexible photoanode paper chip; (g) DFT-calculated band structures and PEC reaction mechanism over the previous reported built-in tandem Z-scheme $MoSe_2$-CdS-ZnO photoanode system. Two parallel internal electric fields (from $MoSe_2$ to CdS and CdS to ZnO) with electron depletion/accumulation layer drive the CB photoexcited electrons of both ZnO and CdS to the VB of CdS and $MoSe_2$, respectively. Reprinted from Ref. 111 with permission. Copyright 2021 Elsevier.

preserving the strong oxidation and reduction capabilities of photogenerated carriers. In essence, a Z-scheme heterojunction refers to a Z-shaped charge transfer pathway following semiconductor photoexcitation, and it is generally categorized into three types: ionic, all-solid-state, and direct Z-scheme heterostructures. The detailed contents are described below.

(Ⅰ) Ionic Z-scheme heterostructures. The concept of the ionic-state Z-scheme heterojunction was first proposed and experimentally demonstrated in 1979. In this configuration (Fig. 7a), the two semiconductors are spatially separated without direct physical contact. Charge transfer between them is mediated by redox shuttle ions, which function as electron mediators. Specifically, the conduction band (CB) electrons of one semiconductor reduce the electron acceptor species, while the valence band (VB) holes of the other semiconductor oxidize the electron donor species, thereby facilitating an indirect recombination process. Consequently, the remaining photogenerated electrons and holes with stronger redox potentials in their respective semiconductors are preserved to participate in water photolysis. Representative redox shuttle couples employed in this system include Fe^{3+}/Fe^{2+}, NO^{-3}/NO^{-2}, IO^{-3}/I^-, $[Co(phen)_3]^{3+/2+}$, $[Co(bpy)_3]^{3+/2+}$, etc.

As a typical TMDs material, WSe_2 is recognized as a p-type semiconductor with high hole mobility and a relatively narrow bandgap of 1.27 eV. In contrast, $SnSe_2$ displays intrinsic n-type conductivity, attributed to its strong electron affinity and the positioning of its Fermi level close to the conduction band minimum. When combined, the $SnSe_2/WSe_2$ heterojunction exhibits an almost broken-gap band alignment, which is particularly advantageous for constructing Z-scheme

heterostructures. For example, Chauhan et al. reported a flexible liquid-exfoliated nanocrystal-based $SnSe_2@WSe_2$ Z-scheme heterojunction photoanode for self-powered PEC conversion, displayed in Fig. 7b and c.[108] This prepared heterojunction photoanode exhibits the considerably improved self-powered photoresponse, 3 times higher than that of individual materials, which predominantly results from their superior visible-light absorption ability and the rapid Z-scheme charge transfer mechanism. According to the provided energy band alignment, the IO^{-3}/I^- redox couple possesses the suitable redox potential of -4.7 eV vs vacuum level, more negative than the CB of $SnSe_2$ and positive than the VB of WSe_2, enabling it feasible as an electron mediator and effectively enhancing the Z-scheme charge transfer between $SnSe_2$ and WSe_2 nanocrystals. Under light irradiation, I^- ions readily scavenge photogenerated holes from the VB of WSe_2, being oxidized to IO^{-3}. Simultaneously, IO^{-3} species are reduced back to I^- by accepting photoexcited electrons from the CB of $SnSe_2$, thereby completing the redox cycle. This reversible IO^{-3}/I^- interconversion promotes efficient charge carrier separation across the heterojunction, accounting for the markedly improved photoelectrochemical performance observed in Fig. 7d.

However, the incorporation of an acceptor–donor pair generally introduces several inherent drawbacks: (ⅰ) carrier migration is hindered due to the involvement of redox mediator diffusion ion pairs; (ⅱ) the mediator itself can interfere with light absorption; (ⅲ) commonly used redox mediators, such as IO^{-3}/I^-, exhibit strong pH sensitivity, thereby narrowing the operational pH window; (ⅳ) numerous irreversible side reactions occur during electron transfer through the mediator; and (ⅴ) the limited
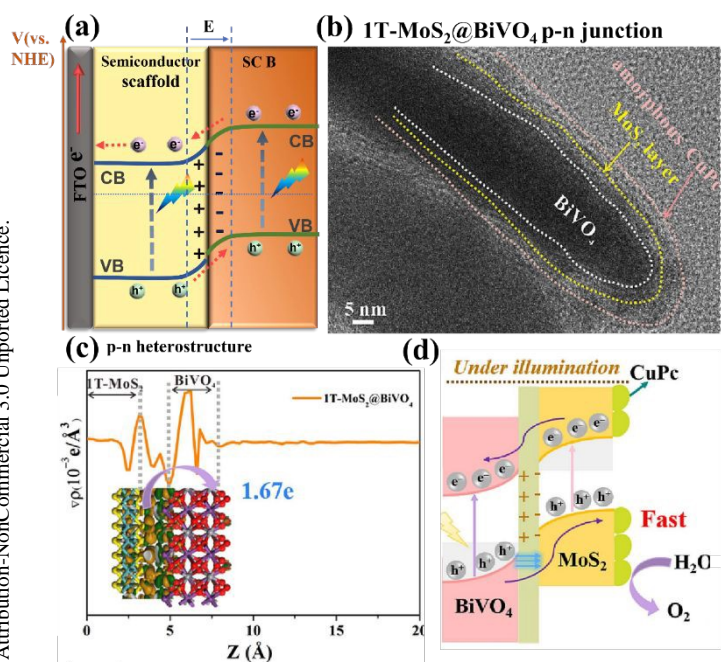
ARTICLE

Fig. 9 (a) Schematic illustration of p-n heterostructure; (b) HRTEM image of the CuPc@1T-MoS$_2$@BiVO$_4$ sample; (c) Planar averaged charge density difference Δρ along the Z direction for the 1T-MoS$_2$@BiVO$_4$ heterostructure; (d) The relevant energy band structure distribution after contact under illumination and the possible charge transfer pathway analysis over the 1T-MoS$_2$@BiVO$_4$ p-n heterostructure photoanode. Reprinted from Ref. 113 with permission. Copyright 2023 Elsevier.

stability of the mediator further constrains the overall reaction rate. To address these limitations, an improved Z-scheme heterostructure of all-solid-state is employed and replaces its function.

(Ⅱ) All-solid-state Z-scheme heterostructures. A representative all-solid-state Z-scheme heterojunction is typically composed of two semiconductor photoabsorbers with appropriately aligned energy bands, bridged by a metallic mediator (Fig. 7e). In this configuration, metallic nanoparticles, such as Au, Ag, Pt, Cu, W, Cd, or conductive materials like reduced graphene oxide (rGO), establish ohmic contacts that are essential for efficient charge transfer. These electron mediators act as recombination centers, enabling the direct annihilation of photogenerated electrons and holes originating from different semiconductors, thereby promoting selective charge separation. Recent studies have highlighted the promising performance of TMDs-based all-solid-state Z-scheme heterostructures for PEC water-splitting, demonstrating their potential to significantly enhance energy conversion efficiency. For example, Hendi et al. reported the preparation of Ag-modified MoS$_2$/RGO/NiWO$_4$ (Ag-MRGON) all-solid-state Z-scheme heterojunction photoanode through all hydrothermal processes.[109] Ag nanoparticles are used as the optical property enhancer to improve the overall photo absorption and rGO serves as the electron mediator to optimize the Z-scheme charge transport routes, suppressing the charge carrier recombination (Fig. 7g). The detailed energy band structures are evaluated by VB-XPS analysis. Under simulated sunlight illumination, photoexcited electrons in CB of NiWO$_4$ transfer and recombine with the VB holes of MoS$_2$ through the

rGO conductive medium, thus efficiently separating and preserving the photogenerated electrons and holes with strong redox capabilities. As a result, the formed Ag-MRGON heterojunction photoanode demonstrates the improved PEC water splitting performance and ABPE conversion efficiency of 0.52%, ~17.3 and ~4.3 times better than those of pure MoS$_2$ and MoS$_2$/NiWO$_4$ photoanodes, together with enhanced photochemical stability of ~2h, as shown in Fig. 7f and S6a-b. More importantly, the fabrication of the all-solid-state Z-scheme heterojunction via the rGO mediator greatly enhances the interfacial water oxidation kinetics, responsible for the cathodically shifted onset potential from 0.73 V$_{RHE}$ (MoS$_2$/NiWO$_4$ heterojunction) to 0.61V$_{RHE}$ (Ag-MRGON). The strategy of all-solid-state Z-scheme heterojunction is effective, but also suffers from the light-shielding effect of the electron mediator and poor long-term stability. Thus, further development is necessary.

(Ⅲ) Direct Z-scheme heterostructures. To advance the practical application of Z-scheme heterojunctions, the concept of the direct Z-scheme system, inspired by natural photosynthesis, has been developed (Fig. 8a). In this configuration, two semiconductors with distinct energy levels are brought into intimate contact, allowing electron redistribution until their Fermi levels are equilibrated. This process establishes a space charge region at the interface, characterized by band bending and an internal electric field. Upon solar irradiation, the built-in electric field facilitates the recombination of conduction band electrons and valence band holes with weaker redox potentials, while the carriers possessing stronger redox potentials remain available to drive the respective water oxidation and reduction half-reactions. Unlike ionic- or all-solid-state-mediated systems, the direct Z-scheme heterojunction eliminates the need for an external mediator, enabling interfacial charge transfer with reduced diffusion distance, enhanced recombination kinetics, and an increased built-in photovoltage. Consequently, this architecture effectively addresses the intrinsic limitations associated with conventional Z-scheme configurations.

The construction of direct Z-scheme heterojunctions requires intimate interfacial contact to ensure efficient charge transfer with minimal resistance, thereby imposing stringent demands on material dimensional control and synthetic methodologies. In recent years, increasing research efforts have been directed toward the development of high-performance TMDs-based direct Z-scheme heterojunction photoanodes for PEC hydrogen evolution, surpassing the focus on their ionic or all-solid-state counterparts. For example, Wen et al. created a type II/Z-scheme MoS$_2$/Bi$_2$S$_3$/Bi$_2$WO$_6$ heterojunction photoanode through the hydrothermal process.[110] As illustrated in Fig. 8b and c, DFT calculation reveals the higher work function of MoS$_2$ (5.746 eV) than Bi$_2$S$_3$ (4.994 eV), and confirms the formation of direct Z-scheme heterojunctions (Fig. 8d). In the presence of irradiation, the photogenerated electrons in CBM of MoS$_2$ trend to recombine with the VBM holes of Bi$_2$S$_3$. Meanwhile, the synergistic effect of type II heterojunction further drives the remaining CBM electrons of Bi$_2$S$_3$ to Bi$_2$WO$_4$, resulting in a significantly extended electron lifetime and the inhibited reassembling of photogenerated charge carriers. As a result, the

ChemComm

ARTICLE

ternary $MoS_2/Bi_2S_3/Bi_2WO_6$ composite photoanode presents excellent PEC performance, achieving a great photocurrent density at around 3.2 mA cm^{-2}, 17.78 times as high as that of pure Bi_2WO_6. Through connecting with a MoS_2-Ni foam photocathode in series, this tandem PEC cell with dual-photoelectrodes manifested an efficient solar-driven hydrogen production with an output of 18.32 μmol/cm^2/h. Li et al. reported a programmable flexible heterojunction photoanode with a built-in tandem Z-scheme configuration, fabricated by in situ growing $MoSe_2$-CdS-ZnO array on Au paper with nanosheet-interlaced-nanorod architectures (Fig. 8e and f).[111] DFT calculation and UPS analysis revealed the relevant bandgap values and double staggered energy band alignment, displayed in Fig. 8g. Photocatalytic degradation of terephthalic acid (TA) and RhB further corroborates the direct Z-scheme charge transport mechanism within the interfaces. Through aligning the Fermi levels of ZnO (0.86 eV), CdS (0.19 eV), and $MoSe_2$ (0.08 eV), two parallel internal electric fields (from $MoSe_2$ to CdS and CdS to ZnO) with electron depletion/accumulation layer near their interface are established, which drive the CB electrons of both ZnO and CdS to the VB of CdS and $MoSe_2$, respectively. Consequently, electrons and holes enrich in the CB of $MoSe_2$ and VB of ZnO with the better redox ability for further PEC reaction. Benefiting from the construction of tandem Z-scheme interfaces (CdS-ZnO and $MoSe_2$-CdS), powerful driving forces are formed to promote rapid charge separation and transfer spatially. Combining with the strengthened optical absorption, photothermal effects, and unique 3D cross-linked network structure, this fabricated $MoSe_2$-CdS-ZnO Z-scheme heterostructure photoanode exhibits admirable PEC HER property (39.7 μmol cm^{-2} h^{-1}). What's more, another convincing case involves the MoO_x/MoS_2/FTO Z-scheme heterostructure photoanode reported by Ghosh et al, which is prepared through the facile solvothermal approach, followed by a two-step annealing technique.[80] The experimental results displays that the formed Z-scheme heterostructure photoanode possesses higher photoresponse and lower charge transfer resistance compared to the pristine MoO_x. All these examples illustrate the appealing superiorities of TMDs-based Z-scheme heterostructure photoanodes in increasing the overall quantum yield and efficiency. However, the construction and characterization of TMDs-based direct Z-scheme heterojunctions photoanodes are still challenging and need further exploration.

4.2.4. p-n and Schottky junctions. Apart from the conventional and Z-scheme heterojunctions discussed above, several alternative TMDs-based nanojunctions have also been developed to enhance the separation and transport of photogenerated charge carriers, including semiconductor p–n junctions and semiconductor/metal Schottky junctions. As presented in Fig. 9a, p-n heterostructure model presents similar energy band alignment with that of Type-Ⅱ configuration, but with the formation of a powerful interfacial built-in electric field, which enables the efficient electron-hole separation across semiconductor junctions. TMDs photoactive materials as promising photoanode candidates show great potential for p-n heterojunction fabrications and have achieved a series of progresses in recent years, mainly including MoS_x/BP/BVO,[112]
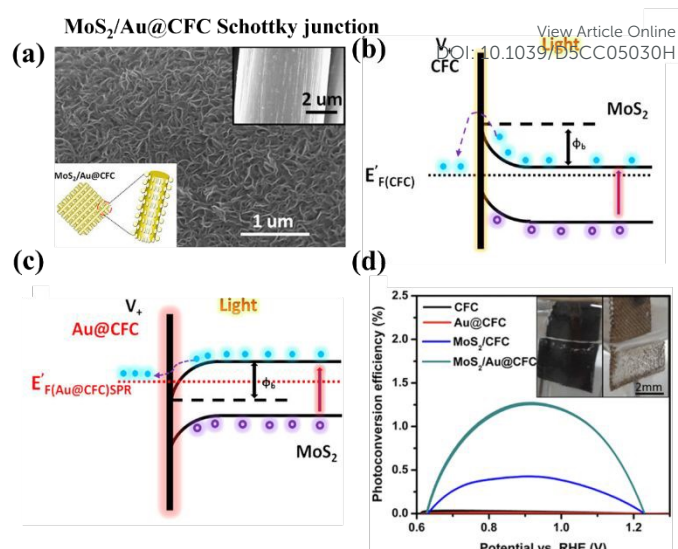

Fig. 10 (a) SEM image of the MoS_2/Au@CFC photoanode; (b, c) Interface energy band structure with charge transfer pathway of the n-type MoS_2/carbon fiber cloth (CFC) Schottky junction and p-type MoS_2/Au@CFC Schottky junction; (d) The calculated ABPE photoconversion efficiencies (%) with a digital photo of PEC O_2 production as the inset, over the previous reported CFC, Au@CFC, MoS_2/CFC, and MoS_2/Au@CFC Schottky junction photoanode systems; Reprinted from Ref. 119 with permission. Copyright 2017 American Chemical Society.

$1T$-MoS_2@$BiVO_4$,[113] WO_3/MoS_2-MoO_x,[114] n-CdS/p-MoS_2,[79] α-Fe_2O_3/MoS_2,[115] MoS_2/NiFe LDH,[116] α-$Fe_2O_3/WS_2/WO_x$,[117] TiO_2 NFs/$1T$@$2H$ $MoSe_2$,[118] etc., p-n junctions. One of the representative examples is related to the $1T$-MoS_2 nanosheets sensitized monoclinic $BiVO_4$ p-n heterojunction photoanodes reported by Yu et l.,[113] which is fabricated through the CVD process (Fig. 9b). DFT calculation and planar charge density difference, shown in Fig. 9c, suggest a strong electron transfer process occurring at $1T$-MoS_2@$BiVO_4$ interface, followed by the formation of a built-in electric potential. Mott-Schottky plots provided confirm the p-type semiconductor characteristic of $1T$-MoS_2, evidencing the formation of p-n junction between $BiVO_4$ and $1T$-MoS_2. Given the corresponding VB-XPS spectra analysis, the staggered energy band configuration and charge transfer energetics are shown in Fig. 9d. Notably, $BiVO_4$ presents a remarkably higher Fermi level than that of $1T$-MoS_2. When the p-type $1T$-MoS_2 layers are conformally deposited onto the n-type $BiVO_4$ film, forming a p–n junction at their interface, the intimate contact between $BiVO_4$ and MoS_2 facilitates interfacial charge redistribution. Benefiting from the superior electrical conductivity and high carrier mobility of metallic phase-MoS_2, the heterostructure offers a stronger driving force for electron transfer. In addition to promoting charge separation, $1T$-MoS_2 also contributes to enhanced light harvesting as an active photo-absorbing component. Consequently, the energy band of $BiVO_4$ bends upward while that of MoS_2 bends downward until the balanced Fermi levels, thereby establishing an internal electric field directed from $BiVO_4$ to MoS_2. Systematic theoretical and experimental studies reveal that introducing a $1T$-MoS_2 interlayer between $BiVO_4$ and the OECs promotes the formation of efficient charge transport pathways for both holes and electrons. As a result, the obtained FeOOH@$1T$-MoS_2@$BiVO_4$ photoelectrode achieves profoundly improved PEC performance and solar conversion

ChemComm Accepted Manuscript

efficiency, with a highest photocurrent density of 4.02 mA cm^{-2} at 1.23 V$_{RHE}$ and optimum ABPE value of 1.28% at 0.68 V$_{RHE}$. Furthermore, the incorporation of copper phthalocyanine (CuPc) can maintain the stable PEC water splitting reaction over 8 h. Recently, TMDs-based Schottky junction photoanodes have also demonstrated their potential for PEC HER applications. For instance, Xu et al. reported the design of a novel Au/MoS$_2$ photoanode for PEC water splitting, which is prepared by first ion sputtering the Au layer on carbon fibre cloth (CFC) substrate, followed by hydrothermal growth of MoS$_2$ nanosheets (Fig. 10a).[119] Through comparing the onset potentials observed from their linear sweep J-V curves (Fig. S7), it is inferred that the photoexcitation of Au plasmons can efficiently modulates the interfacial Schottky barrier. As illustrated in Fig. 10b and c, under illumination, the free electrons of Au oscillating into SPR state possesses the higher energy level than the CB of MoS$_2$, which could rebalance the Fermi levels and change the band bending directions, thus inducing a transition from an n-type to a p-type Schottky junction at interface. This change could greatly promote the electron transfer dynamics, benefiting charge separation and output. As a result, with the embedded Au layer, the prepared MoS$_2$/Au@CFC photoanode exhibits a photocurrent density of 10 mA cm^{-2} at 1.23 V$_{RHE}$ and a maximum ABPE of around 1.27% (Fig. 10d), exceeding a 5-times increase relative to the MoS$_2$@CFC counterpart. A similar result is displayed in the TiO$_2$/(BPEI/MoS$_2$ QDs)n photoanode reported by Lu et al,[120] which is composed of branched polyethylenimine (BPEI) and MoS$_2$ quantum dot (QD) electrostatically assembled on TiO$_2$ nanotube array in a layer-to-layer stacking fashion shown in Fig. S8a. Systematic analysis proves that the introduced MoS$_2$ QDs as a Schottky junction build the cascade electron transfer channel and branched BPEI serves as a directional hole transport channel, synergistically contributing to the accelerated charge separation and prolonged electron lifetimes, then causing the enhanced PEC water splitting (Fig. S8b). The relevant PEC water splitting mechanism over the reported TiO$_2$/(BPEI/MoS$_2$ QDs)n photoanode system is schematically illustrated in Fig. S8c.

As summarized in the above literature and in Table 1, integrating TMDs into Type-I, Type-II, Z-scheme, p-n, and Schottky heterojunctions through rational structural design and interfacial engineering can effectively enhance PEC HER performance by promoting charge separation and transport. Among these configurations, the Type-II heterojunction is the most widely explored owing to its conceptual simplicity and reliable charge-separation capability. However, achieving an optimal balance between efficient carrier transfer dynamics and the preservation of strong redox potentials is still a critical challenge. In contrast, direct Z-scheme heterostructures, although less extensively studied, offer a more architecture innovation in charge transfer channels that eliminates the need for electron mediators and enables superior retention of photogenerated redox power, demonstrating significant promise for practical PEC applications. Nevertheless, the development of scalable synthetic routes and the unambiguous verification of Z-scheme charge-transfer pathways remain major obstacles. Therefore, further intensive research into TMD-based direct Z-scheme heterostructures is

urgently required in future. What's more, beyond charge transfer pathways, TMDs-based heterostructures can also be categorized according to their dimensionality, such as 0D-2D, 1D-2D, 2D-2D, 3D-2D etc. Of focus here is on low-dimensional TMDs materials, particularly their 2D structures, which feature weak interlayer van der Waals interactions and dangling-bond-free surfaces. These characteristics provide significant structural flexibility, allowing free junction with other semiconductor scaffolds without the constraint of lattice mismatch. Therefore, even when composed of identical individual components, TMDs-based heterojunction photoanodes with different dimensional configurations can also exhibit markedly divergent PEC performances. But, in total, the superiority of TMDs-based heterostructures and the positive effects of incorporating TMDs materials, such as enhanced light absorption, established charge transport channels, improved charge separation and transfer, and reinforced photostability, have been well demonstrated in PEC water-splitting applications analysed above.

5. Conclusion and Outlook

PEC water splitting for hydrogen evolution provides a promising approach for directly converting renewable solar energy into green chemical fuels. The current major bottleneck remains still the design and development of highly performing semiconductor photoanodes with simultaneously sufficient spectrum absorption, quantum efficiency, and long-term durability. Low dimensional TMDs photoactive materials, featuring narrow bandgaps, large surface-to-volume atomic ratio, stackability, high charge mobility, short carrier diffusion distance, and excellent photoelectronic properties, are feasible for PEC-HER, targeting scale-up in industrial realization. To address intrinsic limitations such as poor solar utilization and severe carrier recombination, the rational integration of TMDs with complementary semiconductor photoabsorbers to construct heterojunction photoanodes is the focus of current research. This feature article has reviewed the most recent advancements and our contributions in designing and constructing TMDs-based heterostructure photoanodes for optimized PEC hydrogen generation. The unique advantages of TMDs utilization, general heterojunction synthetic strategies (i.e., top-down and bottom-up methods), TMDs-based heterostructure types categorized by charge transfer pathways (including conventional heterostructures, Z-scheme architectures, p–n and Schottky junctions) and distinct dimensionality are summarized in detail. Particular emphasis is placed on the multifaceted roles of TMDs, as photosensitizers, electron-transport mediators, passivation layers, cocatalysts, and protective coatings in optimizing light harvesting, modulating charge-transfer pathways, enhancing charge separation and transport, and improving long-term photostability, within diverse TMDs/SC heterostructure PEC systems, which are discussed separately.

ChemComm

Journal Name

ARTICLE

Table 1 PEC performance comparison of recently reported TMDs-based heterostructure photoanodes.

Charge transfer model	Photocatalysts	Light source and intensity (mV cm^{-2})	Electrolyte	Photocurrent density at 1.23 V$_{RHE}$ (mA cm^{-2})	Onset potential (V$_{RHE}$)	IPCE	ABPE	Ref.
Type- I	CdS/MoS$_2$	AM 1.5G 100	10% lactic acid	1.9 (at 0.8 V$_{RHE}$)	-0.1	45% at 450 nm	N.A.	[33]
Type- I	MoS$_2$/CdS	AM 1.5G 100	0.25 M NaS$_2$ + 0.35 M Na$_2$SO$_3$	2.14 (at 1 V$_{RHE}$)	-0.14	28.1% at 340 nm	N.A.	[32]
Type- I	MoS$_2$/TTZ-COF	AM 1.5G 100	0.1 M Na$_2$SO$_4$	2.5 µA cm^{-2}	~0.6	3.1% at 350 nm	N.A.	[85]
Type- II / Type- I	TiO$_2$/CdS/MoS$_2$	AM 1.5G 100	0.25 M NaS$_2$ + 0.35 M Na$_2$SO$_3$	~3.45 (at 0.9 V$_{RHE}$)	-0.09	45% at 475 nm	N.A.	[78]
Type- II	MoS$_2$/BL-BiVO$_4$	λ ≥ 420 nm 300 W Xe lamp	PPCPs sewage	2.21 (at 1 V$_{Ag/AgCl}$)	0 V$_{Ag/AgCl}$	N.A.	N.A.	[81]
Type- II	E-BiVO$_4$/MoS$_2$	AM 1.5G 100	0.5 M Na$_2$SO$_4$ + 0.1M PBS	2.11	0.36	40.9% at 340 nm	0.53% at 0.77 V$_{RHE}$	[77]
Type- II	W:α-Fe$_2$O$_3$/MoS$_2$	300 W Xe lamp 100	1 M NaOH	1.83	~0.7	38.7% at 325 nm	0.26% at 0.96 V$_{RHE}$	[86]
Type- II	MoS$_2$/WS$_2$	AM 1.5G 100	0.5 M NaClO$_4$	0.45	~0.65	~0.1% at 600 nm	N.A.	[87]
Type- II	MoS$_2$/rGO/Zn-CuInS$_2$	AM 1.5G 100	0.25 M NaS$_2$ + 0.35 M Na$_2$SO$_3$	0.44 (at 0.93 V$_{RHE}$)	~0.15	~6.5% at 375 nm	N.A.	[88]
Type- II	MoS$_2$/WO$_3$	AM 1.5G 100	0.50 M H$_2$SO$_4$	0.96	~0.3	~45% at 320 nm	N.A.	[89]
Type- II	ZnO/MoS$_2$	AM 1.5G 100	0.5 M Na$_2$SO$_4$	2.04	0.37	N.A.	0.67% at ~0.76 V$_{RHE}$	[93]
Type- II	MoS$_2$/WO$_3$	AM 1.5G 100	0.3 M KH$_2$PO$_4$	1.12 (at 0.8 V$_{SCE}$)	~0 V$_{SCE}$	N.A.	0.52% at 0.8 V$_{RHE}$	[90]
Type- II	ZnO/MoS$_2$	AM 1.5G 100	0.5 M Na$_2$SO$_4$	0.61	~0.5	N.A.	0.21% at 0.72 V$_{RHE}$	[94]
Type- II	ZnO/MoS$_2$	150 W Xe lamp 100	0.1 M Na$_2$SO$_4$	1.28 (at 1.65 V$_{RHE}$)	N.A.	N.A.	0.39% at 1.36 V$_{RHE}$	[95]
Type- II	MoS$_2$/a-ZrO$_2$/(010)-BiVO$_4$	AM 1.5G 100	0.5 M Na$_2$SO$_4$	0.6 (at 1.2 V$_{RHE}$)	~0.3	N.A.	N.A.	[82]
Type- II	F−Fe$_2$O$_{3-x}$/MoS$_2$	AM 1.5G 100	1 M NaOH	2.2	~0.8	30.3% at 360 nm	0.21% at 1.04 V$_{RHE}$	[98]
Type- II	MoS$_2$/ZnO/graphene/NF	AM 1.5G 100	0.5 M Na$_2$SO$_3$	0.25 A cm^{-2} (at 1 V$_{Ag/AgCl}$)	0.3	N.A.	5.5% at 0.09 V$_{Ag/AgCl}$	[99]
Type- II	TiO$_{2-x}$-MoS$_2$	AM 1.5G 100	0.5 M Na$_2$SO$_4$+1 M KOH	2.6	~0.55	N.A.	N.A.	[100]
Type- II	Ti-doped WO$_3$–MoS$_2$	150 W Xe lamp	0.5 M Na$_2$SO$_4$	1.15 mA cm^{-2} (at 1.6 V$_{Ag/AgCl}$)	~0.8	0.62% at 400 nm	N.A.	[91]
Type- II	MoS$_2$/GQD/ZnO	AM 1.5G 100	0.5 M Na$_2$SO$_4$	4.36 (at 1.2 V$_{RHE}$)	0.19	N.A.	0.5% at 0.97 V$_{RHE}$	[102]
Type- II	Ag/MoS$_2$/ZnO	AM 1.5G 100	0.5 M Na$_2$SO$_4$	0.7 (at 0 V$_{Ag/AgCl}$)	0.3	N.A.	1.45% at 0.79 V$_{RHE}$	[96]
Type- II	In$_2$S$_3$/MoS$_2$	AM 1.5G 100	0.3 M KH$_2$PO$_4$	1.28	~0.1	~18% at 440 nm	0.75% at 1.23 V$_{RHE}$	[97]
Type- II	MoS$_2$/TiO$_2$/CSF	AM 1.5G 100	0.5 M Na$_2$SO$_4$	33.81	N.A.	N.A.	6.97% at 0.87 V$_{RHE}$	[121]
Type- II	MoS$_2$/TiO$_2$/Au	AM 1.5G 100	0.5 M NaOH	16.3 µA cm^{-2}	N.A.	N.A.	0.34%	[101]
Type- II	TiO$_2$ NFs/MoSe$_2$	AM 1.5G	1 M NaOH	1.4 (at 1.2 V$_{SCE}$)	N.A.	N.A.	N.A.	[118]
Type- II	MoSe$_2$/p$^+$-n Si	AM 1.5G 100	1 M HBr	30 (at 0.8 V$_{RHE}$)	0.3	~75% at 620 nm	13.8% at ~0.5 V$_{RHE}$	[83]
Type- II	WO$_3$/WS$_2$	AM 1.5G 100	0.5 M Na$_2$SO$_4$	5.6 (at 1.23 V$_{Ag/AgCl}$)	~0 V$_{Ag/AgCl}$	55% at 350 nm	2.26% at 0.75 V$_{Ag/AgCl}$	[103]
Type- II	Fe$_2$O$_3$/WS$_2$	AM 1.5G 100	0.5 M NaOH	0.52	0.3	~12.5% at ~420 nm	~0.15% at ~0.8 V$_{RHE}$	[104]
Type- II	CdS/WS$_2$	AM 1.5G 100	0.1 M NaS$_2$ + 0.2 M Na$_2$SO$_3$	3.35 (at 0.4 V$_{SCE}$)	~-1.05	N.A.	~2.64% at ~0 V$_{SCE}$	[105]
Type- II	WS$_2$/TiO$_2$	AM 1.5G 100	0.1 M Na$_2$SO$_4$	2.07 (at 0.7 V$_{SCE}$)	~-0.2 V$_{SCE}$	N.A.	1.52% at 0.32 V$_{SCE}$	[106]
Type- II	WO$_3$@WS$_2$	AM 1.5G	1 M NaOH	0.91	~0.6	N.A.	N.A.	[107]
Ionic Z-scheme	SnSe$_2$/WSe$_2$	150 W Xe lamp	O.5 M NaOH+0.05M KI	0.164 (at 0 V$_{Ag/AgCl}$)	0 V$_{Ag/AgCl}$	N.A.	N.A.	[108]

ChemComm Accepted Manuscript

ARTICLE Journal Name

All solid-state Z-scheme	Ag-MoS$_2$/RGO/NiWO$_4$	AM 1.5G 100	0.5 M Na$_2$SO$_4$	3.5	0.61	N.A.	0.52% at ~1.02 V$_{RHE}$	119
Direct Z-scheme	MoO$_x$/MoS$_2$	AM 1.5G 150	0.5 M H$_2$SO$_4$	2.08 (at 0.9 V$_{RHE}$)	N.A.	N.A.	0.81% at ~0.6 V$_{RHE}$	80

Table 1 (*Contd.*)

Charge transfer model	Photocatalysts	Light source and intensity (mV cm^{-2})	Electrolyte	Photocurrent density at 1.23 V$_{RHE}$ (mA cm^{-2})	Onset potential (V$_{RHE}$)	IPCE	ABPE	Ref.
Direct Z-scheme	MoSe$_2$-CdS-ZnO	AM 1.5G 100	0.55 M NaS$_2$ + 0.127 M Na$_2$SO$_3$	2.4 (at 0.3 V$_{RHE}$)	0	52% at 460 nm	N.A.	111
Type Ⅱ/Z-scheme	MoS$_2$/Bi$_2$S$_3$/Bi$_2$WO$_6$	AM 1.5G	0.5 M PBS + 1 M Na$_2$SO$_3$	3.2	~0.34	16.1% at 432 nm	0.93% at 0.81 V$_{RHE}$	110
p-n junction	FeOOH@1T-MoS$_2$@BiVO$_4$	AM 1.5G 100	0.1M KH$_2$PO$_4$	4.02	~0.1	~78% at 420 nm	1.28% at ~0.62 V$_{RHE}$	122
p-n junction	MoS$_X$/BP/BiVO$_4$	AM 1.5G 100	0.2 M Na$_2$SO$_4$	1.2	N.A.	N.A.	N.A.	112
p-n junction	WO$_3$/MoS$_2$-Mo O$_X$	AM 1.5G 100	0.5 M Na$_2$SO$_4$	2.15	~0.9	27.5% at 375 nm	0.18% at 1 V$_{RHE}$	114
p-n junction	MoS$_2$/CdS	AM 1.5G 80	0.1 M NaS$_2$ + 0.01 M Na$_2$SO$_3$	1.6 (at 0.2 V$_{SCE}$)	N.A.	11% at 440 nm	N.A.	79
p-n junction	α-Fe$_2$O$_3$/MoS$_2$	AM 1.5G 100	1 M NaOH	1.52 mA cm^{-2} (at 0.6 V$_{Ag/AgCl}$)	0.1 V$_{Ag/AgCl}$	7.6% at 325 nm	0.132% at 0.97 V$_{RHE}$	115
p-n junction	MoS$_2$/NiFe LDH	AM 1.5G 100	1 M NaOH	2.6	1.08	26.8% at 420 nm	N.A.	116
p-n junction	a-Fe$_2$O$_3$/WS$_2$/WO$_x$	AM 1.5G 100	1 M NaOH	2.1	0.47	15.5% at 325 nm	0.194% at 0.9 V$_{RHE}$	117
Type-Ⅱ/p-n junction	α-Fe$_2$O$_3$/BiVO$_4$/MoS$_2$	AM 1.5G 100	0.5 M Na$_2$SO$_4$	1.67	~0.3	22% at 325 nm	0.28% at 0.85 V$_{RHE}$	92
Schottky junction	TNTAs/(BPEI–MoS$_2$ QDs)n	AM 1.5G 100	0.5 M Na$_2$SO$_4$	~0.3 (at 0.8 V$_{RHE}$)	~0.2	20.7% at 300 nm	0.16% at ~0.6 V$_{RHE}$	120
Schottky junction	N,S-GQDs/MoSe$_2$	AM 1.5G 100	10% lactic acid	1.8 (at 0.8 V$_{RHE}$)	~0.09	7.62% at 420 nm	N.A.	123
Schottky junction	MoS$_2$/Au@CFC	AM 1.5G 100	0.1 M KH$_2$PO$_4$	10	0.32	~12% at 530 nm	1.27% at ~0.9 V$_{RHE}$	119
Schottky junction	Au-WS$_2$	300 W Xe lamp	1 M Na$_2$SO$_4$	23 (at 1 V$_{SCE}$)	0 V$_{SCE}$	N.A.	N.A.	124

Despite notable progress and increasing research interest, the development of TMDs heterostructure photoanode for PEC water splitting remains at an early stage and has yet to meet the performance benchmarks required for practical industrial application. Considerable efforts and broader design considerations are still required to realize a reliable alternative PEC device. Firstly, achieving a well-defined heterostructurewith the clear structure-activity relationship is essential, as the thickness of TMDs affects both their energy band structure and charge diffusion distance, which determines their suitability for high-performance PEC applications. Concurrently, the development of robust synthetic strategies enabling the controllable fabrication of TMDs-based heterostructures with scalability, high crystallinity, and cost-effectiveness is crucial for their commercialization. Secondly, strengthened fundamental research on the interfacial connections and properties of low-dimensional TMDs-based heterostructures is of great importance. To deepen understanding, model systems with atomic-scale precision and atomically sharp interfaces based on advanced spectroscopic techniques and DFT computations are highly required, enabling elucidation of interfacial mechanisms, optimization of heterostructure design, and enhancement of device performance. Thirdly, although 1T-phase TMDs typically exhibit superior catalytic activity compared to their 2H-phase counterparts, they suffer from inherent instability under ambient conditions and during photoreaction processes. Therefore, future research should prioritize strategies to stabilize the 1T phase, such as electron-donor doping (Re, V), intercalation, noble-metal mediated SPR hot-electron injection, and other advanced phase-engineering approaches.[125-128] These efforts will be crucial for fully exploiting the catalytic potential of 1T-phase TMDs in PEC applications. Fourth, interfacial adhesion between TMDs and semiconductor scaffolds could be further enhanced through substrate surface activation (plasma/UV-ozone) or nanoscale texturing, interlayer engineering (ultrathin oxides or functional polymer) and chemical functionalization for strengthening the junction chemical bonding, reducing interface defect, and promoting coherent heterojunction formation. Meanwhile, employing conformal encapsulation of OER cocatalysts, such as transition metal-based oxides, MOF, phosphates or supramolecular cocatalysts, to isolate TMDs from electrolyte, avoid intercalation, and optimize hole extraction is critical to mitigating degradation and photocorrosion, thereby improving their photostability.[129-132] Or, further exploration of suitable organic sacrificial agents, as alternatives to conventional hole scavengers (e.g., Na$_2$S/Na$_2$SO$_3$), is feasible to rationally utilize surface holes for producing high-value-added chemicals while

ARTICLE

synchronously accomplishing stable hydrogen evolution. Finally, future efforts should also focus on the development of TMD-based heterostructure photoanode–photocathode configurations or photovoltaic–photoelectrochemical (PV-PEC) tandem architectures to enable unassisted solar water splitting. Integrating these photoelectrodes with state-of-the-art photovoltaic technologies, such as TOPCon Si, perovskites, and CZTS, in dual- or multi-junction layouts, or designing monolithically integrated tandem devices with sufficiently high STH efficiencies and long-term operational stability,[133] represents a promising and essential direction for advancing practical PEC systems, which is also a key focus of our future research. In summary, our efforts will continue in developing highly efficient TMDs-based and other heterostructure photoanodes with enhanced solar harvesting, optimized charge dynamics, and prolonged stability. We hope this feature article could inspire further innovation in the design of advanced TMDs-based van der Waals heterojunction photoelectrodes for next-generation PEC catalysis.

Author contributions

Zhiyuan Peng and **Yilu Su** contributed equally. **Zhiyuan Peng:** Conceptualization, Investigation, Writing-original draft. **Yilu Su**: Conceptualization, Writing-original draft. **Imane En-Naji:** Investigation, Visualization. **Amir Khojastehnezhad:** Visualization. **Mohamed Siaj:** Funding acquisition, Resources, Supervision, Writing- review and editing.

Data availability

No primary research results, software or code have been included and no new data were generated or analysed as part of this review.

Conflicts of interest

There are no conflicts to declare.

Acknowledgements

References

1 J. H. Kim, D. Hansora, P. Sharma, J.-W. Jang and J. S. Lee, *Chem. Soc. Rev.*, 2019, **48**, 1908-1971.
2 S. E. Hosseini and M. A. Wahid, *Renew. Sustain. Energy Rev.*, 2016, **57**, 850-866.
3 M. Bullock and K. More, *Basic energy sciences roundtable: foundational science for carbon-neutral hydrogen technologies*, USDOE Office of Science (SC), Basic Energy Sciences (BES), 2021.
4 M. Grätzel, *nature*, 2001, **414**, 338-344.
5 H. Song, S. Luo, H. Huang, B. Deng and J. Ye, *ACS Energy Lett.*, 2022, **7**, 1043-1065.
6 H. Wu, L. Zhang, A. Du, R. Irani, R. van de Krol, F. F. Abdi and Y. H. Ng, *Nat. Commun.*, 2022, **13**, 6231.
7 T.-G. Vo, C.-C. Kao, J.-L. Kuo, C.-c. Chiu and C.-Y. Chiang, *Appl. Catal. B Environ.*, 2020, **278**, 119303.
8 D. Voiry, J. Yang and M. Chhowalla, *Adv. Mater.*, 2016, **28**, 6197-6206.
9 M. Chhowalla, H. S. Shin, G. Eda, L.-J. Li, K. P. Loh and H. Zhang, *Nat. Chem.*, 2013, **5**, 263-275.
10 X. Yu, N. Guijarro, M. Johnson and K. Sivula, *Nano Lett.*, 2018, **18**, 215-222.
11 M. Xu, T. Liang, M. Shi and H. Chen, *Chem. Rev.*, 2013, **113**, 3766-3798.
12 X. Huang, Z. Zeng and H. Zhang, *Chem. Soc. Rev.*, 2013, **42**, 1934-1946.
13 V. H. Nguyen, T. P. Nguyen, T. H. Le, D. V. N. Vo, D. L. Nguyen, Q. T. Trinh, I. T. Kim and Q. V. Le, *J. Chem. Technol. Biotechnol.*, 2020, **95**, 2597-2607.
14 A. Hannan, A. Khalil, N. Arshad, M. B. Tahir, A. G. Wattoo and M. K. Shahzad, *Energy Technol.*, 2022, **10**, 2200546.
15 X. Zheng, Z. Guo, G. Zhang, H. Li, J. Zhang and Q. Xu, *J. Mater. Chem. A*, 2019, **7**, 19922-19928.
16 M. Faraji, M. Yousefi, S. Yousefzadeh, M. Zirak, N. Naseri, T. H. Jeon, W. Choi and A. Z. Moshfegh, *Energy Environ. Sci.*, 2019, **12**, 59-95.
17 C. Li, Q. Cao, F. Wang, Y. Xiao, Y. Li, J.-J. Delaunay and H. Zhu, *Chem. Soc. Rev.*, 2018, **47**, 4981-5037.
18 J. Liu, Z. Luo, X. Mao, Y. Dong, L. Peng, D. Sun‑Waterhouse, J. V. Kennedy and G. I. Waterhouse, *Small*, 2022, **18**, 2204553.
19 M. G. Walter, E. L. Warren, J. R. McKone, S. W. Boettcher, Q. Mi, E. A. Santori and N. S. Lewis, *Chem. Rev.*, 2010, **110**, 6446-6473.
20 L. Clarizia, M. N. Nadagouda and D. D. Dionysiou, *Curr. Opin. Green Sustainable Chem.*, 2023, **41**, 100825.
21 J. Jia, L. C. Seitz, J. D. Benck, Y. Huo, Y. Chen, J. W. D. Ng, T. Bilir, J. S. Harris and T. F. Jaramillo, *Nat. Commun.*, 2016, **7**, 13237.
22 W. Yang, R. R. Prabhakar, J. Tan, S. D. Tilley and J. Moon, *Chem. Soc. Rev.*, 2019, **48**, 4979-5015.
23 J. Fu, Z. Fan, M. Nakabayashi, H. Ju, N. Pastukhova, Y. Xiao, C. Feng, N. Shibata, K. Domen and Y. Li, *Nat. Commun.*, 2022, **13**, 729.
24 E. Nurlaela, Y. Sasaki, M. Nakabayashi, N. Shibata, T. Yamada and K. Domen, *J. Mater. Chem. A*, 2018, **6**, 15265-15273.
25 H. Hajibabaei, D. J. Little, A. Pandey, D. Wang, Z. Mi and T. W. Hamann, *ACS Appl. Mater. Interfaces*, 2019, **11**, 15457-15466.
26 P. Boddy, *J. Electrochem. Soc.*, 1968, **115**, 199.
27 A. Fujishima and K. Honda, *nature*, 1972, **238**, 37-38.
28 W.-H. Cheng, M. H. Richter, M. M. May, J. Ohlmann, D. Lackner, F. Dimroth, T. Hannappel, H. A. Atwater and H.-J. Lewerenz, *ACS Energy Lett.*, 2018, **3**, 1795-1800.
29 Y. Tachibana, L. Vayssieres and J. R. Durrant, *Nat. Photonics*, 2012, **6**, 511-518.
30 M. T. Mayer, *Curr. Opin. Electrochem.*, 2017, **2**, 104-110.
31 K. Peng, X. Wang and S.-T. Lee, *Appl. Phys. Lett.*, 2008, **92**.
32 Z. Peng, Y. Su, M. Jafari and M. Siaj, *J. Mater. Sci. Technol.*, 2023, **167**, 107-118.
33 T. A. Ho, C. Bae, J. Joe, H. Yang, S. Kim, J. H. Park and H. Shin, *ACS Appl. Mater. Interfaces*, 2019, **11**, 37586-37594.
34 L. Clarizia, D. Spasiano, I. Di Somma, R. Marotta, R. Andreozzi and D. D. Dionysiou, *Int. J. Hydrogen Energy*, 2014, **39**, 16812-16831.
35 C. Jiang, S. J. Moniz, A. Wang, T. Zhang and J. Tang, *Chem. Soc. Rev.*, 2017, **46**, 4645-4660.
36 Y. Zhao, Z. Niu, J. Zhao, L. Xue, X. Fu and J. Long, *Electrochem. Energy Rev.*, 2023, **6**, 14.

View Article Online
DOI: 10.1039/D5CC05080H

37 H. Zhang, D. Li, W. J. Byun, X. Wang, T. J. Shin, H. Y. Jeong, H. Han, C. Li and J. S. Lee, *Nat. Commun.*, 2020, **11**, 4622.

38 V. K. Khanna, *Eur. J. Phys.*, 2004, **25**, 221.

39 C. Xu, H. Wang, H. Guo, K. Liang, Y. Zhang, W. Li, J. Chen, J. S. Lee and H. Zhang, *Nat. Commun.*, 2024, **15**, 9712.

40 K. Kang, C. Tang, J. H. Kim, W. J. Byun, J. H. Lee, M. H. Lee, H. Zhang and J. S. Lee, *ACS Catal.*, 2023, **13**, 7002-7012.

41 K. Sivula, F. L. Formal and M. Gratzel, *Chem. Mater.*, 2009, **21**, 2862-2867.

42 L. M. Peter, K. U. Wijayantha and A. A. Tahir, *Faraday Discuss.*, 2012, **155**, 309-322.

43 W. W. Gärtner, *Phys. Rev.*, 1959, **116**, 84-87.

44 L. K. Dhandole, H. H. Lee, W.-S. Chae, J. S. Jang and J. S. Lee, *J. Energy Chem.*, 2022, **65**, 415-423.

45 K. Sivula, R. Zboril, F. Le Formal, R. Robert, A. Weidenkaff, J. Tucek, J. Frydrych and M. Gratzel, *J. Am. Chem. Soc.*, 2010, **132**, 7436-7444.

46 Y. Zhang, Y. Li, D. Ni, Z. Chen, X. Wang, Y. Bu and J. P. Ao, *Adv. Funct. Mater.*, 2019, **29**, 1902101.

47 Y. Su, Z. Peng, E.-N. Imane, P. Liu, A. Khojastehnezhad, J. Claverie and M. Siaj, *ACS Appl. Nano Mater.*, 2025, **8**, 14689-14702.

48 P. Liu, A. Dorfler, A. A. Tabrizi, L. Skokan, D. Rawach, P. Wang, Z. Peng, J. Zhang, A. P. Ruediger and J. P. Claverie, *ACS Appl. Mater. Interfaces*, 2023, **15**, 27832-27844.

49 J. Gangwar, B. K. Gupta, S. K. Tripathi and A. K. Srivastava, *Nanoscale*, 2015, **7**, 13313-13344.

50 Z. Peng, J. Zhang, P. Liu, J. Claverie and M. Siaj, *ACS Appl. Mater. Interfaces*, 2021, **13**, 34658-34670.

51 Z. Peng, Y. Su and M. Siaj, *Appl. Catal. B Environ.*, 2023, **330**, 122614.

52 X. Zhou, J. Wu, Y. Xiao, Y. Jiang, W. Zhang, Y. Liu, Z. Liu and J. Zhang, *Sep. Purif. Technol.*, 2023, **311**, 123243.

53 Y. Xiao, Y. Jiang, E. Zhou, W. Zhang, Y. Liu, J. Zhang, X. Wu, Q. Qi and Z. Liu, *J. Mater. Sci. Technol.*, 2023, **153**, 205-218.

54 F. Chen, Z. Deng, X. Li, J. Zhang and J. Zhao, *Chem. Phys. Lett.*, 2005, **415**, 85-88.

55 H. Wang, L. Zhang, Z. Chen, J. Hu, S. Li, Z. Wang, J. Liu and X. Wang, *Chem. Soc. Rev.*, 2014, **43**, 5234-5244.

56 D. Li, R. Wei, H. Yin, H. Zhang, X. Wang and C. Li, *Chem. Sci.*, 2023, **14**, 1861-1870.

57 M. G. Lee, J. W. Yang, I. J. Park, T. H. Lee, H. Park, W. S. Cheon, S. A. Lee, H. Lee, S. G. Ji and J. M. Suh, *Carbon Energy*, 2023, **5**, e321.

58 Q. Cao, J. Yu, K. Yuan, M. Zhong and J.-J. Delaunay, *ACS Appl. Mater. Interfaces*, 2017, **9**, 19507-19512.

59 S. Zhao, B. Liu, K. Li, S. Wang, G. Zhang, Z.-J. Zhao, T. Wang and J. Gong, *Nat. Commun.*, 2024, **15**, 2970.

60 D. Voiry, A. Mohite and M. Chhowalla, *Chem. Soc. Rev.*, 2015, **44**, 2702-2712.

61 S. Shi, Z. Sun and Y. H. Hu, *J. Mater. Chem. A*, 2018, **6**, 23932-23977.

62 J. Kang, S. Tongay, J. Zhou, J. Li and J. Wu, *Appl. Phys. Lett.*, 2013, **102**.

63 R. J. Toh, Z. Sofer, J. Luxa, D. Sedmidubský and M. Pumera, *Chem. Commun.*, 2017, **53**, 3054-3057.

64 J. Xie, H. Zhang, S. Li, R. Wang, X. Sun, M. Zhou, J. Zhou, X. W. Lou and Y. Xie, *Adv. Mater.*, 2013, **25**, 5807-5813.

65 J. N. Coleman, M. Lotya, A. O'Neill, S. D. Bergin, P. J. King, U. Khan, K. Young, A. Gaucher, S. De and R. J. Smith, *Science*, 2011, **331**, 568-571.

66 N. Martín, N. Tagmatarchis, Q. H. Wang and X. Zhang, *Chem. - Eur. J.*, 2020, **26**, 6292-6295.

67 A. R. Brill, E. Koren and G. de Ruiter, *J. Mater. Chem. C*, 2021, **9**, 11569-11587.

68 S. Manzeli, A. Allain, A. Ghadimi and A. Kis, *Nano Lett.*, 2015, **15**, 5330-5335.

69 Y. Gong, Z. Liu, A. R. Lupini, G. Shi, J. Lin, S. Najmaei, Z. Lin, A. L. Elías, A. Berkdemir and G. You, *Nano Lett.*, 2014, **14**, 442-449.

70 B. Radisavljevic, A. Radenovic, J. Brivio, V. Giacometti and A. Kis, *Nat. Nanotechnol.*, 2011, **6**, 147-150.

71 H. Abdullah, H. Shuwanto, J. Lie and M. Sillanpää, *J. Environ. Chem. Eng.*, 2023, **11**, 109356.

72 H. Li, J. Wu, Z. Yin and H. Zhang, *Acc. Chem. Res.*, 2014, **47**, 1067-1075.

73 M. Wang, S. Osella, R. Brescia, Z. Liu, J. Gallego, M. Cattelan, M. Crisci, S. Agnoli and T. Gatti, *Nanoscale*, 2023, **15**, 522-531.

74 D. B. Seo, J. Kim, Y. M. Jo, D. I. Kim, T. G. Lim, S. Kang, S. Yim, S. S. Lee, E. T. Kim and K. S. An, *Energy Environ. Mater.*, 2025, **8**, e70055.

75 K. Roy, S. Maitra, D. Ghosh, P. Kumar and P. Devi, *Chem. Eng. J.*, 2022, **435**, 134963.

76 J. B. Naceur, R. B. Zaghouani, M. Amlouk, M. A. Zaabi and R. Chtourou, *Inorg. Chem. Commun.*, 2023, **147**, 110270.

77 Z. Peng, Y. Su, I. Ennaji, A. Khojastehnezhad and M. Siaj, *Chem. Eng. J.*, 2023, **477**, 147082.

78 S. S. Bhat, S. A. Pawar, D. Potphode, C.-K. Moon, J. M. Suh, C. Kim, S. Choi, D. S. Patil, J.-J. Kim and J. C. Shin, *Appl. Catal. B Environ.*, 2019, **259**, 118102.

79 A. Pareek, H. G. Kim, P. Paik and P. H. Borse, *J. Mater. Chem. A*, 2017, **5**, 1541-1547.

80 D. Ghosh, P. Devi, O. S. Kushwaha, R. Kumar and P. Kumar, *ACS Appl. Energy Mater.*, 2020, **3**, 6834-6844.

81 Z. Zheng and I. M. Lo, *Appl. Catal. B Environ.*, 2021, **299**, 120636.

82 H. Zhao, X. Wei, R. Gu, M. Xie and W. Han, *Appl. Phys. Lett.*, 2024, **125**.

83 S. Vanka, Y. Wang, P. Ghamari, S. Chu, A. Pandey, P. Bhattacharya, I. Shih and Z. Mi, *Sol. RRL*, 2018, **2**, 1800113.

84 J. Wang, Y. Peng, T. Zhou, J. Fu, W. Quan, Y. Cheng, H. Ding and Y. Zhang, *Small*, 2025, 2407233.

85 Z. Zhou, P. Li, X. Gao, J. Chen, K. Akhtar, E. M. Bakhsh, S. B. Khan, Y. Shen and M. Wang, *J. Environ. Chem. Eng.*, 2022, **10**, 106900.

86 Z. Masoumi, M. Tayebi, M. Kolaei, A. Tayyebi, H. Ryu, J. I. Jang and B.-K. Lee, *ACS Appl. Mater. Interfaces*, 2021, **13**, 39215-39229.

87 F. M. Pesci, M. S. Sokolikova, C. Grotta, P. C. Sherrell, F. Reale, K. Sharda, N. Ni, P. Palczynski and C. Mattevi, *ACS Catal.*, 2017, **7**, 4990-4998.

88 F. Li, D. Benetti, M. Zhang, L. Shi, J. Feng, Q. Wei and F. Rosei, *ACS Appl. Mater. Interfaces*, 2022, **14**, 54790-54802.

89 Y.-H. Xiao and W.-D. Zhang, *Electrochim. Acta*, 2017, **252**, 416-423.

90 D.-B. Seo, V. Dongquoc, R. A. Jayarathna, S. Lee, J.-H. Lee and E.-T. Kim, *J. Alloys Compd.*, 2022, **911**, 165090.

91 J. Yadav, A. Phutela, J. A. Khan, S. Bhattacharya and J. Singh, *Int. J. Hydrogen Energy*, 2024, **79**, 826-838.

92 Z. Masoumi, M. Tayebi, M. Kolaei and B.-K. Lee, *J. Alloys Compd.*, 2022, **890**, 161802.

93 K. Karmakar, D. Maity, D. Pal, K. Mandal and G. G. Khan, *ACS Appl. Nano Mater.*, 2020, **3**, 1223-1231.

94 A. R. Fareza, L. Roza, F. A. A. Nugroho and V. Fauzia, *Surf. Interfaces*, 2023, **37**, 102663.

95 P. Shinde, Y. Hase, V. Doiphode, B. R. Bade, D. Kale, S. Rahane, J. Thombare, D. Borkar, S. R. Rondiya and M. Prasad, *ACS Appl. Energy Mater.*, 2025, **8**, 935-948.

96 M. Chia, W. Chiu, P. Khiew, N. Chanlek, H. Lee, C. Haw, R. Abd-Shukor and M. A. A. Hamid, *CrystEngComm*, 2025, **27**, 749-761.

97 R. A. Jayarathna, J.-H. Heo and E.-T. Kim, *Nanomaterials*, 2024, **14**, 1628.

98 J. Wu, M. Meng, X.-D. Du, M. Li, L. Jin and W. Liu, *Inorg. Chem.*, 2024, **63**, 6192-6201.

99   N. N. Rosman, N. R. A. M. Shah, S. N. F. Moridon, K. Arifin, L. J. Minggu, N. A. Ludin and R. M. Yunus, *Int. J. Hydrogen Energy*, 2025, **104**, 324-335.

100   M. Rezaei, A. A. Ensafi and E. Heydari-Bafrooei, *J. Ind. Eng. Chem.*, 2025, **146**, 589-602.

101   H.-B. Do, L. D. Pham, T. X. Phan, W.-Z. Chen, L.-W. Lan, H.-J. Lin, V.-H. Nguyen, C.-L. Dong, A. S. Kumar and A. F. El-Mahdy, *Nanotechnology*, 2024, **35**, 385703.

102   F. Khodabandeh, H. Abdizadeh and M. R. Golobostanfard, *ACS Appl. Energy Mater.*, 2024, **8**, 170-180.

103   M. Tayebi, Z. Masoumi and B.-K. Lee, *Ultrason. Sonochem.*, 2021, **70**, 105339.

104   G. C. Behera, B. Biswal, J. K. Bidika, B. R. K. Nanda, S. Alwarappan, J. K. Rath and S. C. Roy, *Small*, 2025, **21**, 2406715.

105   S. Ladhane, S. Shah, V. Doiphode, P. Shinde, D. Kale, S. Rahane, J. Thombare, M. Ingole, P. Vairale and Y. Hase, *J. Power Sources*, 2025, **656**, 238056.

106   S. Ladhane, S. Shah, V. Doiphode, P. Shinde, A. Punde, D. Kale, S. Rahane, J. Thombare, Y. Hase and A. Waghmare, *Mater. Chem. Phys.*, 2025, **334**, 130440.

107   J. Lai, B. Wang, Y. Gong, C. Sun, W. Wang and W. Yang, *RSC Adv.*, 2023, **13**, 4150-4155.

108   P. Chauhan, A. B. Patel, G. Solanki, H. K. Machhi, C. Sumesh, S. S. Soni, V. Patel and V. Pathak, *J. Phys. Chem. C*, 2021, **125**, 14729-14740.

109   A. H. Hendi, A. M. Osman, I. Khan, T. A. Saleh, T. A. Kandiel, T. F. Qahtan and M. K. Hossain, *ACS omega*, 2020, **5**, 31644-31656.

110   A. Wan, Z. Ren, Y. He, Y. Zhang, S. Zhang, M. Tu, J. Li and M. Qiu, *Appl. Surf. Sci.*, 2025, **690**, 162607.

111   L. Li, H. Shi, H. Yu, X. Tan, Y. Wang, S. Ge, A. Wang, K. Cui, L. Zhang and J. Yu, *Appl. Catal. B Environ.*, 2021, **292**, 120184.

112   Y. Xu, X. Zhang, Z. Chen, K. Kempa, X. Wang and L. Shui, *J. Mater. Sci. Technol.*, 2021, **68**, 1-7.

113   L. Yu, K. Xue, H. Luo, C. Liu, H. Liu, H. Zhu and Y. Zhang, *Chem. Eng. J.*, 2023, **472**, 144965.

114   M. Tayebi, Z. Masoumi, M. Kolaei, A. Tayyebi, M. Tayebi, B. Seo, C.-S. Lim, H.-G. Kim and B.-K. Lee, *Chem. Eng. J.*, 2022, **446**, 136830.

115   Z. Masoumi, M. Tayebi and B.-K. Lee, *Ultrason. Sonochem.*, 2021, **72**, 105403.

116   X. Yang, J. Sun, H. Fu, J. Chen, J. Fan, X. Tong, X. Ran and X. An, *Powder Technol.*, 2024, **431**, 119051.

117   Z. Masoumi, M. Tayebi, M. Kolaei and B.-K. Lee, *Appl. Catal. B Environ.*, 2022, **313**, 121447.

118   H. Li, C. Yang, X. Wang, J. Zhang, J. Xi, G. Du and Z. Ji, *J. Am. Ceram. Soc.*, 2020, **103**, 1187-1196.

119   X. Xu, G. Zhou, X. Dong and J. Hu, *ACS Sustainable Chem. Eng.*, 2017, **5**, 3829-3836.

120   Z.-Q. Wei, X.-C. Dai, S. Hou, Y.-B. Li, M.-H. Huang, T. Li, S. Xu and F.-X. Xiao, *J. Mater. Chem. A*, 2020, **8**, 177-189.

121   H. Cho, J.-Y. Kim, D. S. Shin, J. S. Lee, J. Shim, I.-H. Lee, W. K. Choi, N. Kwon, S. Park and M. S. Yazici, *Adv. Sensor Energy Mater.*, 2024, **3**, 100088.

122   L. Yu, K. Xue, H. Luo, C. Liu, H. Liu, H. Zhu and Y. Zhang, *Chem. Eng. J.*, 2023, **472**, 144965.

123   L. Zhang, J. Sun, M. Zhao, Y. Wei, T. Luo, Z. Zhao and Y. Yan, *Molecules*, 2024, **29**, 1070.

124   G. Bharath, K. Rambabu, B. Alqassem, P. P. Morajkar, M. A. Haija, A. K. Nadda, V. K. Gupta and F. Banat, *Chem. Eng. J.*, 2023, **456**, 141062.

125   Q. Liu, X. Li, Q. He, A. Khalil, D. Liu, T. Xiang, X. Wu and L. Song, *Small*, 2015, **11**, 5556-5564.

126   A. N. Enyashin, L. Yadgarov, L. Houben, I. Popov, M. Weidenbach, R. Tenne, M. Bar-Sadan and G. Seifert, *J. Phys. Chem. C*, 2011, **115**, 24586-24591.

127   X. Sun, J. Dai, Y. Guo, C. Wu, F. Hu, J. Zhao, X. Zeng and Y. Xie, *Nanoscale*, 2014, **6**, 8359-8367.

128   Y. Liu, W. Huang, W. Chen, X. Wang, J. Guo, H. Tian, H. Zhang, Y. Wang, B. Yu and T.-L. Ren, *Appl. Surf. Sci.*, 2019, **481**, 1127-1132.

129   L. Liardet, J. E. Katz, J. Luo, M. Grätzel and X. Hu, *J. Mater. Chem. A*, 2019, **7**, 6012-6020.

130   J. B. Pan, B. H. Wang, J. B. Wang, H. Z. Ding, W. Zhou, X. Liu, J. R. Zhang, S. Shen, J. K. Guo and L. Chen, *Angew. Chem. Int. Ed.*, 2021, **60**, 1433-1440.

131   G. Liu, Y. Zhao, R. Yao, N. Li, M. Wang, H. Ren, J. Li and C. Zhao, *Chem. Eng. J.*, 2019, **355**, 49-57.

132   J. Miao, C. Lin, X. Yuan, Y. An, Y. Yang, Z. Li and K. Zhang, *Nat. Commun.*, 2024, **15**, 2023.

133   G. Jung, C. Moon, F. Martinho, Y. Jung, J. Chu, H. Park, A. Hajijafarassar, R. Nielsen, J. Schou and J. Park, *Adv. Energy Mater.*, 2023, **13**, 2301235.

ChemComm Accepted Manuscript

Data Availability Statement

No primary research results, software or code have been included and no new data were generated or analyzed as part of this review.

Low-dimensional transition metal dichalcogenides heterostructure photoanodes for photoelectrochemical hydrogen evolution application: Recent progress and prospects

Zhiyuan Peng,[a,†] Yilu Su,[b,†] Imane En-Naji,[a] Amir Khojastehnezhad [a] and Mohamed Siaj [a,*]

a. Faculty of Engineering, Université de Sherbrooke, 2500 Blvd de l'Université, Sherbrooke, QC, J1K 2R1, Canada

b. Department of Chemistry, Université du Québec à Montréal, Montréal, QC, H3C 3P8, Canada

† These authors contributed equally.

* Corresponding author, E-mail: mohamed.siaj@usherbrooke.ca; Tel: +1 514 987000 # 1921